INTERNATIONAL JOURNAL FOR NUMERICAL METHODS IN ENGINEERING
Int. J. Numer. Meth. Engng 0000; **00**:1–26
Published online in Wiley InterScience (www.interscience.wiley.com). DOI: 10.1002/nme

Analytical study of the accuracy of discrete element simulations

K. J. Hanley[1]* and C. O'Sullivan[2]

[1] *Institute for Infrastructure and Environment, School of Engineering, The University of Edinburgh, Edinburgh EH9 3JL, UK*
[2] *Department of Civil and Environmental Engineering, Skempton Building, Imperial College London, London SW7 2AZ, UK*

SUMMARY

The numerical errors in idealised discrete element method (DEM) simulations are investigated analytically by comparing energy balances applied at the beginning and end of one time-step. This study focuses on the second-order velocity-Verlet integration scheme due to its widespread implementation in DEM codes. The commercial DEM software PFC2D was used to verify the correctness of key results. The truncation errors, which are larger than the round-off errors by orders of magnitude, have a superlinear relationship with both the simulation time-step and the interparticle collision speed. This remains the case regardless of simulation details including the chosen contact model, particle size distribution, particle density or stiffness. Hence, the total errors can usually be reduced by choosing a smaller time-step. Increasing the polydispersity in a simulation by including smaller particles necessitates choosing a smaller time-step to maintain simulation stability and reduces the truncation errors in most cases. The truncation errors are increased by the dissipation of energy by frictional sliding or by the inclusion of damping in the system. The number of contacts affects the accuracy and one can deduce that because 2D simulations contain fewer interparticle contacts than the equivalent 3D simulations, they therefore have lower accrued simulation errors. Copyright © 0000 John Wiley & Sons, Ltd.

Received . . .

KEY WORDS: validation; discrete element method; granular media; particle methods; time integration, explicit

1. INTRODUCTION

Since its development in the 1970s [1,2], the discrete element method (DEM) has become extremely popular as a tool for investigating the particle-scale behaviour of granular materials in science and engineering. Many researchers have conducted numerical simulations to establish how the simulation conditions and input parameters (e.g., the contact model [3, 4], the number of particles [5–7] or the interparticle friction coefficient [8–10]) affect simulation results such as the observed load–deformation response. This aim of this study is to investigate how the choices made in a DEM

*Correspondence to: Kevin Hanley, Institute for Infrastructure and Environment, School of Engineering, The University of Edinburgh, Edinburgh EH9 3JL, UK. E-mail: k.hanley@ed.ac.uk

Copyright © 0000 John Wiley & Sons, Ltd.

simulation affect its accuracy and therefore the reliability of the result: a subject which has received little academic attention to date. DEM simulations are dynamic and there will inevitably be errors associated with temporal discretization in the time integration algorithm. There may also be errors due to spatial discretization.

The error generated in one step of any numerical method can be divided into two categories: truncation error or round-off error [11]. The sum of all errors from previous steps is sometimes called the inherited error [12]. Truncation errors occur when a limited number of terms are used to approximate the infinite number required for an exact representation (e.g., Taylor series are often represented by fewer than five terms). Round-off errors occur because computers use a finite number of digits to represent numbers: an exact representation of an irrational number such as π would require infinitely-many digits. Round-off errors are usually smaller than truncation errors by orders of magnitude. This study focuses primarily on truncation errors as round-off errors are less significant and are also hardware- and implementation-specific, depending on factors including the representation chosen for floating-point numbers and the number of arithmetic operations performed.

The approach adopted in this study is to initially quantify the truncation error for the simplest possible 'base case': the normal impact of two identical frictionless spheres with a linear contact model. The truncation error is quantified by comparing energy balances applied to the idealised system at the beginning and end of one time-step. Energy balances have been used previously in studies of DEM simulation accuracy [13, 14] and more generally to check the correctness of DEM code implementations [15, 16]. Energy balances are often used for similar purposes in other computational methods such as the finite element method [17]. Other approaches to quantify error have been adopted in DEM, particularly the comparison of simulation outputs with analytical solutions [18–21]; however, the versatility of an approach based on energy balances favoured its adoption for this study.

The truncation error depends on the integration scheme chosen [13, 19–21]. This study is based on the second-order velocity-Verlet integration scheme as it is a good compromise between accuracy and computational efficiency [13]. Furthermore, this integration scheme has been widely adopted in DEM codes including the open-source codes LAMMPS [22], LIGGGHTS [23], Yade [24] and MercuryDPM [25, 26], although other schemes are also in use (e.g., PFC2D/3D use a related Verlet-based scheme [27, 28]). Once the base case has been established, it is adapted in many ways, including by choosing dissimilar particles, by changing contact model, by permitting the development of shear forces and the dissipation of energy by friction, by including damping or interparticle bonds in the model formulation, and by introducing multiple simultaneous contacts. All of these analyses are done symbolically using the Maple 17.00 software [29]. The effect of simulation time-step and density scaling on error are quantified analytically and discussed. Key expressions obtained for the truncation error are verified by comparing with the results of PFC2D simulations [30].

The aim of this paper is to identify and show the relative importance of those factors which affect the truncation error. This is achieved by focusing on small, idealised systems and analysing a single time-step only. Because the accrued error is generally path-dependent, the total accrued truncation error in a large simulation cannot be estimated by multiplying the error for one time-step and one interparticle contact by both the number of time-steps and contacts. However, it might be inferred

Copyright © 0000 John Wiley & Sons, Ltd.

Prepared using nmeauth.cls
DOI: 10.1002/nme

that any actions identified to reduce the truncation error for a single contact and time-step, e.g., changing the particle density, would similarly reduce the unknown total accrued error in a large simulation.

2. MATHEMATICAL ANALYSIS OF THE BASIC TWO-PARTICLE DEM

The fundamental velocity-Verlet equations for a particle α of mass m with no angular velocity are (1–4), in which $\boldsymbol{v}$, $\boldsymbol{f}$ and $\boldsymbol{x}$ refer to translational velocity, force or displacement, respectively; n and s superscripts are used to distinguish normal and shear/tangential components of contact force, and subscripts refer to accrued simulation time, t, and the simulation time-step, Δt. In a typical implementation, (1) and (2) are executed at the beginning of the time-step, then the net forces are updated (3) which is usually the most computationally-expensive part of the calculation, before (4) is executed at the end of the time-step.

$$\boldsymbol{v}_{\alpha,t+\frac{\Delta t}{2}} = \boldsymbol{v}_{\alpha,t} + \frac{\Delta t}{2m}\,\boldsymbol{f}_{\alpha,t} \tag{1}$$

$$\boldsymbol{x}_{\alpha,t+\Delta t} = \boldsymbol{x}_{\alpha,t} + \Delta t\,\boldsymbol{v}_{\alpha,t+\frac{\Delta t}{2}} \tag{2}$$

$$\boldsymbol{f}_{\alpha,t+\Delta t} = \boldsymbol{f}_{\alpha,t} + \boldsymbol{f}^{n}_{\alpha,t+\Delta t} + \boldsymbol{f}^{s}_{\alpha,t+\Delta t} \tag{3}$$

$$\boldsymbol{v}_{\alpha,t+\Delta t} = \boldsymbol{v}_{\alpha,t+\frac{\Delta t}{2}} + \frac{\Delta t}{2m}\,\boldsymbol{f}_{\alpha,t+\Delta t} \tag{4}$$

2.1. *Truncation error for base case*

The simplest possible 'base case' is the normal impact of two identical frictionless spheres with a linear contact model, as illustrated in Figure 1. At a time t, the particles are in touching contact with no overlap ($\boldsymbol{f}_{\alpha,t} = \boldsymbol{f}_{\beta,t} = 0$). Particle α has a velocity $\boldsymbol{v}_{\alpha,t} = \boldsymbol{v}_i$ while particle β is at rest ($\boldsymbol{v}_{\beta,t} = 0$). During the time-step $t \to t + \Delta t$, an overlap, and hence a normal contact force, is developed while the shear force remains zero.

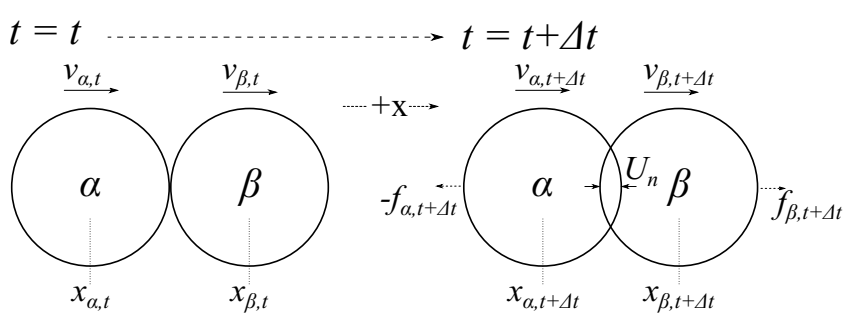

Figure 1. Schematic of the two-particle base case, showing an initial touching contact at time t and the development of an overlap by time $t + \Delta t$.

As there is no mechanism for energy dissipation in this system, (5) represents an energy balance applied to the system at times t and $t + \Delta t$.

$$E^{K}_{\alpha,t} = E^{K}_{\alpha,t+\Delta t} + E^{K}_{\beta,t+\Delta t} + E^{NS}_{t+\Delta t} - \epsilon \tag{5}$$

Copyright © 0000 John Wiley & Sons, Ltd.

DOI: 10.1002/nme

The K and NS superscripts denote the kinetic energy and the normal component of strain energy, respectively. ϵ represents the truncation error; the negative contribution of error to (5) implies a net generation of energy during this time-step as expected from [15, 18]. The energy terms can be substituted by

$$E^K_{\alpha,t} = \frac{1}{2}\, m\, |\boldsymbol{v}_i|^2 \tag{6}$$

$$E^K_{\alpha,t+\Delta t} = \frac{1}{2}\, m\, |\boldsymbol{v}_{\alpha,t+\Delta t}|^2 \tag{7}$$

$$E^K_{\beta,t+\Delta t} = \frac{1}{2}\, m\, |\boldsymbol{v}_{\beta,t+\Delta t}|^2 \tag{8}$$

$$E^{NS}_{t+\Delta t} = \frac{|\boldsymbol{f}^n_{\alpha,t+\Delta t}|^2}{2\, k_n}\ . \tag{9}$$

For this case, $\boldsymbol{f}^n_{\alpha,t+\Delta t} = -\boldsymbol{f}^n_{\beta,t+\Delta t}$. (9) is applicable only to a linear, Hookean contact model with a constant spring stiffness k_n. For a linear contact model, $\boldsymbol{f}^n_{\alpha,t+\Delta t} = -k_n\, \boldsymbol{U}_n$ where $\boldsymbol{U}_n$ is the interparticle overlap. After substituting (6–9) into (5),

$$\frac{1}{2}\, m\, |\boldsymbol{v}_i|^2 = \frac{1}{2}\, m\, |\boldsymbol{v}_{\alpha,t+\Delta t}|^2 + \frac{1}{2}\, m\, |\boldsymbol{v}_{\beta,t+\Delta t}|^2 + \frac{|\boldsymbol{f}^n_{\alpha,t+\Delta t}|^2}{2\, k_n} - \epsilon\ . \tag{10}$$

Since the particles are initially in touching contact, and using (1) and (2),

$$\begin{aligned} \boldsymbol{U}_n &= (\boldsymbol{x}_{\beta,t} - \boldsymbol{x}_{\alpha,t}) - (\boldsymbol{x}_{\beta,t+\Delta t} - \boldsymbol{x}_{\alpha,t+\Delta t}) \\ &= \Delta t \left(\boldsymbol{v}_{\alpha,t+\frac{\Delta t}{2}} - \boldsymbol{v}_{\beta,t+\frac{\Delta t}{2}} \right) \\ &= \Delta t\, \boldsymbol{v}_i\ . \end{aligned} \tag{11}$$

Substituting for $\boldsymbol{v}_{\alpha,t+\Delta t}$ and $\boldsymbol{v}_{\beta,t+\Delta t}$ in (10) using (1) and (4),

$$\frac{1}{2}\, m\, |\boldsymbol{v}_i|^2 = \frac{1}{2}\, m \left| \boldsymbol{v}_i + \frac{\Delta t}{2m}\, \boldsymbol{f}_{\alpha,t+\Delta t} \right|^2 + \frac{1}{2}\, m \left| \frac{\Delta t}{2m}\, \boldsymbol{f}_{\beta,t+\Delta t} \right|^2 + \frac{|\boldsymbol{f}^n_{\alpha,t+\Delta t}|^2}{2\, k_n} - \epsilon\ . \tag{12}$$

$\boldsymbol{f}^s_{\alpha,t+\Delta t} = \boldsymbol{f}^s_{\beta,t+\Delta t} = 0$ and $\boldsymbol{f}^n_{\alpha,t+\Delta t} = -\boldsymbol{f}^n_{\beta,t+\Delta t}$; therefore, $\boldsymbol{f}_{\alpha,t+\Delta t} = -\boldsymbol{f}_{\beta,t+\Delta t} = \boldsymbol{f}^n_{\alpha,t+\Delta t}$. This substitution is made in (12). Noting also that $\boldsymbol{v}_i$ and $\boldsymbol{f}^n_{\alpha,t+\Delta t}$ differ in sign,

$$\begin{aligned} 0 &= m \left| \frac{\Delta t}{2m}\, \boldsymbol{f}^n_{\alpha,t+\Delta t} \right|^2 - \frac{1}{2}\, |\boldsymbol{v}_i|\, \Delta t\, |\boldsymbol{f}^n_{\alpha,t+\Delta t}| + \frac{|\boldsymbol{f}^n_{\alpha,t+\Delta t}|^2}{2\, k_n} - \epsilon \\ \epsilon &= \frac{|\boldsymbol{f}^n_{\alpha,t+\Delta t}|}{2} \left(\frac{|\boldsymbol{f}^n_{\alpha,t+\Delta t}|\, \Delta t^2}{2m} - |\boldsymbol{v}_i|\, \Delta t + \frac{|\boldsymbol{f}^n_{\alpha,t+\Delta t}|}{k_n} \right)\ . \end{aligned} \tag{13}$$

Recall that $\boldsymbol{f}^n_{\alpha,t+\Delta t} = -k_n\, \boldsymbol{U}_n = -k_n\, \Delta t\, \boldsymbol{v}_i$. Hence,

$$\begin{aligned} \epsilon &= \frac{k_n\, \Delta t\, |\boldsymbol{v}_i|}{2} \left(\frac{k_n\, \Delta t^3\, |\boldsymbol{v}_i|}{2m} - |\boldsymbol{v}_i|\, \Delta t + |\boldsymbol{v}_i|\, \Delta t \right) \\ \epsilon &= \frac{k_n^2\, |\boldsymbol{v}_i|^2\, \Delta t^4}{4m}\ . \end{aligned} \tag{14}$$

Copyright © 0000 John Wiley & Sons, Ltd.

DOI: 10.1002/nme

(14) indicates that the truncation error in one time-step, expressed in terms of energy, has a quadratic relationship with both normal spring stiffness and collision speed (which is related to strain rate for a dense granular system). The truncation error is inversely proportional to particle mass and has a fourth-order dependence on the simulation time-step.

(14) implies that the truncation error can be reduced by increasing particle mass relative to the stiffness – either by increasing the diameter or the density. However, Δt cannot be chosen arbitrarily; a limitation of Verlet-based integration schemes is conditional stability which is contingent on adopting a time-step lower than the critical time-step. If the time-step chosen for a simulation is too large, the instability is often manifested by a non-physical generation of energy which may be detected by means of an energy balance [31]. The stable time-step for linear, undamped systems using a central difference time integration scheme is usually set as a multiple of the critical time-step for an idealised system [28,32–34] which depends on particle mass. This stable time-step, Δt_s, is given by (15) where η is a constant:

$$\Delta t_s = \eta \sqrt{\frac{m}{k_n}} \,. \tag{15}$$

Substituting (15) into (14), the truncation error when $\Delta t = \Delta t_s$ is $\epsilon_s \propto m\,|\boldsymbol{v}_i|^2$. Hence, assuming that the simulation time-step is chosen using the conventional approach (15), the truncation error is directly proportional to particle mass for these linear systems. ϵ is positive indicating an increase in energy during a loading time-step.

If the initial relative velocity of $\boldsymbol{v}_i$ is partitioned differently between the particles, e.g., if particle α has a velocity $\boldsymbol{v}_{\alpha,t} = \frac{\boldsymbol{v}_i}{2}$ and particle β has a velocity $\boldsymbol{v}_{\beta,t} = -\frac{\boldsymbol{v}_i}{2}$, it is straightforward to show that the truncation error is unchanged. Thus ϵ is independent of the manner in which the relative velocity is partitioned among the colliding particles.

2.2. *Effect of dissimilar particles on truncation error*

The particles in Section 2.1 have identical masses, m. However, the particles could have different masses, m_α and m_β, because of a difference in size and/or density. Adopting the same approach as in Section 2.1 except distinguishing between m_α and m_β,

$$\frac{1}{2}\,m_\alpha\,|\boldsymbol{v}_i|^2 = \frac{1}{2}\,m_\alpha\,|\boldsymbol{v}_{\alpha,t+\Delta t}|^2 + \frac{1}{2}\,m_\beta\,|\boldsymbol{v}_{\beta,t+\Delta t}|^2 + \frac{\left|\boldsymbol{f}^n_{\alpha,t+\Delta t}\right|^2}{2\,k_n} - \epsilon \,.$$

This distinction is also made in (1) and (4) when substituting for $\boldsymbol{v}_{\alpha,t+\Delta t}$ and $\boldsymbol{v}_{\beta,t+\Delta t}$. The truncation error becomes

$$\epsilon = \frac{k_n^2\,|\boldsymbol{v}_i|^2\,\Delta t^4 (m_\alpha + m_\beta)}{8\,m_\alpha\,m_\beta} \,. \tag{16}$$

(14) is recovered by substituting $m_\alpha = m_\beta = m$ into (16). As in Section 2.1, the initial distribution of relative velocity among the particles does not affect the truncation error, i.e., whether the heavier particle has the greater or lesser speed does not affect ϵ. The truncation error is minimised for identical particles; as the particle masses become increasingly dissimilar, the truncation error increases non-linearly. This is best demonstrated by imposing the following two restrictions on m_α

Copyright © 0000 John Wiley & Sons, Ltd.

DOI: 10.1002/nme

and m_β where C is a constant and $R \leq 1$:

$$m_\alpha + m_\beta = C \qquad\qquad \frac{m_\alpha}{m_\beta} = R\,.$$

Figure 2a is a plot of ϵ, normalised by the truncation error at $R = 1$ (i.e., 14), against R. The curve in Figure 2a has the analytical form $\frac{(R+1)^2}{4\,R\,C^2}$. The error is unbounded as $R \to 0$. This analysis disregards the dependence of time-step on particle mass. For systems containing particles of differing masses, (15) remains applicable but it is commonplace for the mass in (15) to be chosen conservatively as the minimum particle mass: m_α in this case. Substituting for Δt in (16), $\epsilon_s \propto C\,R\,|\boldsymbol{v}_i|^2$ as plotted in Figure 2b. The direct proportionality of ϵ_s and C again indicates that increasing the particle masses will degrade the accuracy of a simulation time-step. Increasing the polydispersity by including smaller particle sizes reduces the truncation error in a time-step, provided that the size of this time-step is chosen according to (15).

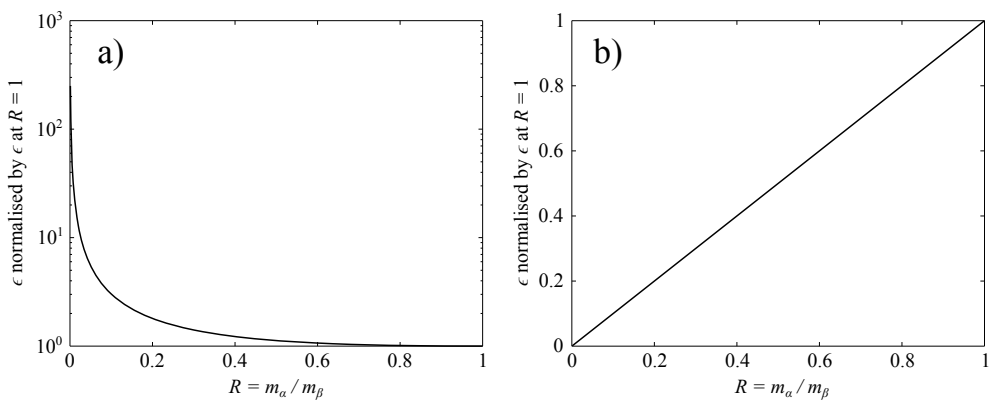

Figure 2. The non-dimensionalised truncation error in one time-step for a linear, undamped, two-particle system. (a) ignores the dependence of time-step on particle mass while (b) assumes a time-step proportional to $\sqrt{m_\alpha/k_n}$.

2.3. *Effect of contact model on truncation error*

Many simulations of real materials use contact models based on Hertzian mechanics rather than a simple linear model. $\boldsymbol{f}^n_{\alpha,t+\Delta t}$ and $E^{NS}_{t+\Delta t}$ may be found for a Hertzian contact using

$$\boldsymbol{f}^n_{\alpha,t+\Delta t} = -\boldsymbol{f}^n_{\beta,t+\Delta t} = -H_n\,\boldsymbol{U}_n^{\frac{3}{2}} \tag{17}$$

$$E^{NS}_{t+\Delta t} = \frac{2}{5}\,|\boldsymbol{U}_n\,\boldsymbol{f}^n_{\alpha,t+\Delta t}| \tag{18}$$

where H_n is a function of the particle radii (r_α and r_β), shear modulus (G) and Poisson's ratio (ν):

$$H_n = \frac{4\,G}{3\,(1-\nu)}\sqrt{\frac{r_\alpha\,r_\beta}{r_\alpha + r_\beta}}\,. \tag{19}$$

Copyright © 0000 John Wiley & Sons, Ltd.

DOI: 10.1002/nme

(18) is substituted into (5) as for the linear contact model. A distinction is made between m_α and m_β in (20) and particle α is assumed to possess all of the initial kinetic energy:

$$\frac{1}{2}\,m_\alpha\,|\boldsymbol{v}_i|^2 = \frac{1}{2}\,m_\alpha\,|\boldsymbol{v}_{\alpha,t+\Delta t}|^2 + \frac{1}{2}\,m_\beta\,|\boldsymbol{v}_{\beta,t+\Delta t}|^2 + \frac{2}{5}\,|\boldsymbol{U}_n\,\boldsymbol{f}^n_{\alpha,t+\Delta t}| - \epsilon\,. \tag{20}$$

A similar back-substitution procedure is adopted as before, using (17) to substitute for normal contact force where necessary. As in Sections 2.1 and 2.2, an expression for the truncation error in the energy balance, ϵ, may be obtained as a function of known simulation parameters. This expression is expressed most concisely as

$$\epsilon = \frac{H_n^2\,|\boldsymbol{v}_i|^3\,\Delta t^5(m_\alpha + m_\beta)}{8\,m_\alpha\,m_\beta} - \frac{1}{10}\,H_n\,(\Delta t\,|\boldsymbol{v}_i|)^{\frac{5}{2}} \tag{21}$$

which simplifies to the following when $m_\alpha = m_\beta = m$:

$$\epsilon = \frac{H_n^2\,|\boldsymbol{v}_i|^3\,\Delta t^5}{4\,m} - \frac{1}{10}\,H_n\,(\Delta t\,|\boldsymbol{v}_i|)^{\frac{5}{2}}\;. \tag{22}$$

(21) contains a mixture of masses and radii (within H_n). (21) may be written purely in terms of mass by replacing r_α and r_β with $\sqrt[3]{\frac{3\,m_\alpha}{4\,\pi\,\rho}}$ and $\sqrt[3]{\frac{3\,m_\beta}{4\,\pi\,\rho}}$, respectively, assuming particles α and β have the same density, ρ. The truncation error is independent of the manner in which the relative velocity is partitioned among the colliding particles, as was the case for a linear contact model. Both of the terms in (21) contain shear modulus, time-step and collision speed in their numerators, indicating that the magnitude of the truncation error generally increases with these factors. If the first term, proportional to the fifth power of time-step, is negligible in comparison with the second term, then the magnitude of the error is independent of particle density. There is a non-trivial time-step (23) at which $\epsilon = 0$:

$$\Delta t_{\epsilon=0} = \left(\frac{4\,m_\alpha\,m_\beta}{5\,H_n\sqrt{|\boldsymbol{v}_i|}\,(m_\alpha + m_\beta)}\right)^{\frac{2}{5}}\;. \tag{23}$$

The increased complexity of (21) compared with (16) makes it difficult to ascertain whether ϵ increases or decreases in magnitude when the degree of polydispersity is increased. In fact, either scenario is possible depending on the parameters chosen for the model. The following input parameters were selected to illustrate this: $\rho = 2650\,\mathrm{kg\,m^{-3}}$, $G = 0.2\,\mathrm{Pa}$, $\nu = 0.2$, $C = 1.388 \times 10^{-6}\,\mathrm{kg}$ and $\Delta t = 0.01\,\mathrm{s}$. $|\boldsymbol{v}_i|$ was varied between $0.1\,\mathrm{m\,s^{-1}}$ and $500\,\mathrm{m\,s^{-1}}$ while R was varied between 0.001 and 1. The chosen simulation time-step of 0.01 s is stable at all R and was calculated based on Rayleigh wave transmission [35], applying a factor of safety of ten to the calculated critical time-step. Figure 3 shows the variation of truncation error with R and collision speed.

When the collision speed is large ($\geq 50\,\mathrm{m\,s^{-1}}$), $|\epsilon|$ increases non-linearly with increasing polydispersity, as seen for a similar linear system in Figure 2. However, a transition in behaviour occurs at smaller collision speeds whereby increasing polydispersity, i.e., decreasing R, reduces the magnitude of the error until some transition point is reached (e.g., $R = 0.17$ when $|\boldsymbol{v}_i| = 10\,\mathrm{m\,s^{-1}}$). This transition point is marked by a change of sign: $\epsilon > 0$ to the left of this transition point whereas $\epsilon < 0$ above this value. The reason for this transition is apparent from (21). At large collision speeds, the first term dominates ($\propto |\boldsymbol{v}_i|^3$) so $\epsilon > 0$. As the collision speed decreases, the negative second

Copyright © 0000 John Wiley & Sons, Ltd.

DOI: 10.1002/nme

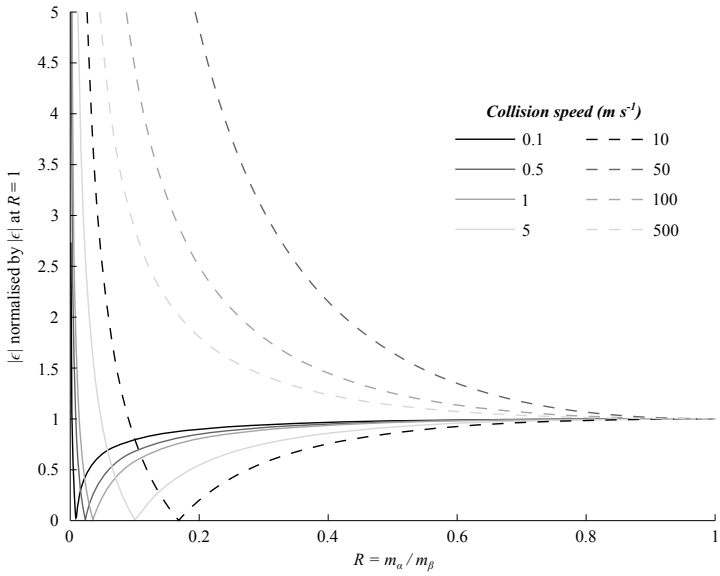

Figure 3. The absolute values of the truncation errors in one time-step, non-dimensionalised by the value for two identical particles ($R = 1$) for an undamped, frictionless two-particle system with a Hertzian contact model in which the collision speed is varied from $0.1\,\mathrm{m\,s^{-1}}$ to $500\,\mathrm{m\,s^{-1}}$.

term ($\propto |\boldsymbol{v}_i|^{\frac{5}{2}}$) becomes increasingly significant, causing ϵ to become negative for a larger range of R. In Figure 3, the time-step is the same for all R. In practice, Δt is a function of the minimum particle diameter (15): if R is increased by including smaller particles in the simulation, Δt must be reduced. This analysis indicates that increasing the polydispersity of a simulation will usually reduce ϵ because of the strong dependence of ϵ on Δt.

2.4. *Considering shear forces between frictional particles: linear contact model*

Real particles are frictional and shear forces can be developed at interparticle contacts. Most DEM codes use simple Coulomb-type friction. The base case developed in Section 2.1 was modified to permit the development of shear forces by allocating particle α an initial angular velocity, $\boldsymbol{\omega}_{\alpha,t} = \boldsymbol{\omega}_i$, in addition to a translational velocity, $\boldsymbol{v}_i$. Figure 4 shows the modified two-particle schematic. Compared to the base case, the problem is two-dimensional rather than one-dimensional.

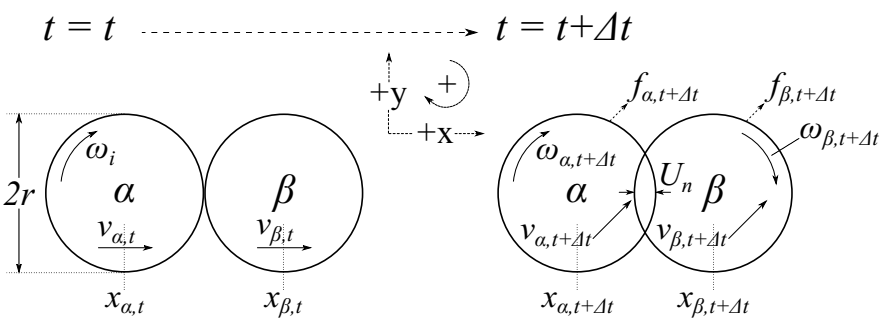

Figure 4. A modification of the two-particle base case in Figure 1 to include an initial non-zero angular velocity of particle α.

Copyright © 0000 John Wiley & Sons, Ltd.

DOI: 10.1002/nme

The complete set of velocity-Verlet equations for particle α is

$$\boldsymbol{v}_{\alpha,t+\frac{\Delta t}{2}} = \boldsymbol{v}_{\alpha,t} + \frac{\Delta t}{2m}\,\boldsymbol{f}_{\alpha,t} \tag{24}$$

$$\boldsymbol{\omega}_{\alpha,t+\frac{\Delta t}{2}} = \boldsymbol{\omega}_{\alpha,t} + \frac{5\Delta t}{4mr^2}\,\boldsymbol{M}_{\alpha,t} \tag{25}$$

$$\boldsymbol{x}_{\alpha,t+\Delta t} = \boldsymbol{x}_{\alpha,t} + \Delta t\,\boldsymbol{v}_{\alpha,t+\frac{\Delta t}{2}} \tag{26}$$

$$\boldsymbol{f}_{\alpha,t+\Delta t} = \boldsymbol{f}_{\alpha,t} + \boldsymbol{f}^n_{\alpha,t+\Delta t} + \boldsymbol{f}^s_{\alpha,t+\Delta t} \tag{27}$$

$$\boldsymbol{v}_{\alpha,t+\Delta t} = \boldsymbol{v}_{\alpha,t+\frac{\Delta t}{2}} + \frac{\Delta t}{2m}\,\boldsymbol{f}_{\alpha,t+\Delta t} \tag{28}$$

$$\boldsymbol{\omega}_{\alpha,t+\Delta t} = \boldsymbol{\omega}_{\alpha,t+\frac{\Delta t}{2}} + \frac{5\Delta t}{4mr^2}\,\boldsymbol{M}_{\alpha,t+\Delta t}\,. \tag{29}$$

Particles α and β remain collinear at time $t+\Delta t$. Therefore, the normal and shear components of contact force act in the x- and y-directions, respectively. As for the base case, $\boldsymbol{f}^n_{\alpha,t+\Delta t} = -\boldsymbol{f}^n_{\beta,t+\Delta t}$ and similarly $\boldsymbol{f}^s_{\alpha,t+\Delta t} = -\boldsymbol{f}^s_{\beta,t+\Delta t}$. $\boldsymbol{M}$ refers to moment or torque acting on a particle. This can be calculated as the product of the shear force and the displacement of the contact point from the particle centroid:

$$\boldsymbol{M}_{\alpha,t+\Delta t} = \boldsymbol{f}^s_{\alpha,t+\Delta t}\left(\frac{\boldsymbol{x}_{\beta,t+\Delta t} - \boldsymbol{x}_{\alpha,t+\Delta t}}{2}\right) \tag{30}$$

$$\boldsymbol{M}_{\beta,t+\Delta t} = \boldsymbol{f}^s_{\beta,t+\Delta t}\left(\frac{\boldsymbol{x}_{\alpha,t+\Delta t} - \boldsymbol{x}_{\beta,t+\Delta t}}{2}\right)\,. \tag{31}$$

$\boldsymbol{M}_{\alpha,t+\Delta t} = \boldsymbol{M}_{\beta,t+\Delta t}$ since both the shear forces acting on particles α and β and the displacements of the contact point from the centroids differ only in sign. Both moments are negative which implies that $\boldsymbol{\omega}_{\alpha,t+\Delta t} < \boldsymbol{\omega_i}$ and $\boldsymbol{\omega}_{\beta,t+\Delta t} < 0$. $\boldsymbol{M}_{\alpha,t} = \boldsymbol{M}_{\beta,t} = 0$ as the shear forces are zero at time t.

Normal forces are always calculable from the positions of the particle centroids whereas shear forces require incremental calculation. This important distinction is unnecessary in this special case of a simulation consisting of one time-step. Although it is not explored in this paper, the calculation of shear forces incrementally is inherently much less accurate than the calculation of normal forces. The shear force for this analysis is calculated as the product of the contact shear stiffness, k_s, and the increment of shear displacement during the time-step $t \to t+\Delta t$, $\boldsymbol{U}_s$. $\boldsymbol{U}_s$ is solely due to the initial angular velocity, $\boldsymbol{\omega}_i$:

$$\boldsymbol{f}^s_{\alpha,t+\Delta t} = -k_s\,\boldsymbol{U}_s = -k_s\,\boldsymbol{\omega}_i\,\Delta t\left(\frac{\boldsymbol{x}_{\beta,t+\Delta t} - \boldsymbol{x}_{\alpha,t+\Delta t}}{2}\right)\,. \tag{32}$$

The shear force acting on particle α is negative, giving a negative moment (30) to oppose the positive initial angular velocity. The energy balance corresponding to Figure 4 is

$$E^K_{\alpha,t} = E^K_{\alpha,t+\Delta t} + E^K_{\beta,t+\Delta t} + E^{NS}_{t+\Delta t} + E^{SS}_{t+\Delta t} + E^F_{t+\Delta t} - \epsilon\,. \tag{33}$$

$E^{SS}_{t+\Delta t}$ is the strain energy stored in the shear spring and $E^F_{t+\Delta t}$ is the energy dissipated by frictional sliding during the time-step $t \to t+\Delta t$. If a linear contact model is used with a shear stiffness k_s

Copyright © 0000 John Wiley & Sons, Ltd.

DOI: 10.1002/nme

and the particles have the same radius, r,

$$E^K_{\alpha,t} = \frac{1}{2}\, m\, |\boldsymbol{v}_i|^2 + \frac{1}{5}\, m\, r^2\, |\boldsymbol{\omega}_i|^2 \tag{34}$$

$$E^K_{\alpha,t+\Delta t} = \frac{1}{2}\, m\, |\boldsymbol{v}_{\alpha,t+\Delta t}|^2 + \frac{1}{5}\, m\, r^2\, |\boldsymbol{\omega}_{\alpha,t+\Delta t}|^2 \tag{35}$$

$$E^K_{\beta,t+\Delta t} = \frac{1}{2}\, m\, |\boldsymbol{v}_{\beta,t+\Delta t}|^2 + \frac{1}{5}\, m\, r^2\, |\boldsymbol{\omega}_{\beta,t+\Delta t}|^2 \tag{36}$$

$$E^{NS}_{t+\Delta t} = \frac{\left|\boldsymbol{f}^n_{\alpha,t+\Delta t}\right|^2}{2\, k_n} \tag{9}$$

$$E^{SS}_{t+\Delta t} = \frac{\left|\boldsymbol{f}^s_{\alpha,t+\Delta t}\right|^2}{2\, k_s}\,. \tag{37}$$

The energy dissipated by Coulomb friction is described by a piecewise function governed by the interparticle friction coefficient, μ [28]. Once frictional sliding occurs, the shear force is reduced in magnitude from $|\boldsymbol{f}^s_{\alpha,t+\Delta t}|$ to $\mu\left|\boldsymbol{f}^n_{\alpha,t+\Delta t}\right|$. In (38), $\overline{\boldsymbol{f}^s_{t+\Delta t}}$ is the average of the shear forces at the beginning and end of the time-step (after rescaling) while $\boldsymbol{U}^s_s$ is the slip displacement at the contact.

$$E^F_{t+\Delta t} = \begin{cases} 0 & \text{if } \left|\boldsymbol{f}^s_{\alpha,t+\Delta t}\right| \leq \mu\left|\boldsymbol{f}^n_{\alpha,t+\Delta t}\right| \\ \left|\overline{\boldsymbol{f}^s_{t+\Delta t}}\,\boldsymbol{U}^s_s\right| & \text{if } \left|\boldsymbol{f}^s_{\alpha,t+\Delta t}\right| > \mu\left|\boldsymbol{f}^n_{\alpha,t+\Delta t}\right| \end{cases} \tag{38}$$

Initially, let us assume that $E^F_{t+\Delta t} = 0$. (33) becomes

$$\begin{aligned} \frac{1}{2}\, m\, |\boldsymbol{v}_i|^2 + \frac{1}{5}\, m\, r^2\, |\boldsymbol{\omega}_i|^2 &= \frac{1}{2}\, m\, |\boldsymbol{v}_{\alpha,t+\Delta t}|^2 + \frac{1}{5}\, m\, r^2\, |\boldsymbol{\omega}_{\alpha,t+\Delta t}|^2 \\ &\quad + \frac{1}{2}\, m\, |\boldsymbol{v}_{\beta,t+\Delta t}|^2 + \frac{1}{5}\, m\, r^2\, |\boldsymbol{\omega}_{\beta,t+\Delta t}|^2 + \frac{\left|\boldsymbol{f}^n_{\alpha,t+\Delta t}\right|^2}{2\, k_n} + \frac{\left|\boldsymbol{f}^s_{\alpha,t+\Delta t}\right|^2}{2\, k_s} - \epsilon\,. \end{aligned} \tag{39}$$

Following the same approach as in Section 2.1, (24–32) are simplified and successively substituted into (39) to leave ϵ as a function of $|\boldsymbol{v}_i|$, $|\boldsymbol{\omega}_i|$, k_n, k_s, r and Δt:

$$\epsilon = \frac{k_n^2\, |\boldsymbol{v}_i|^2\, \Delta t^4}{4m} + \frac{k_s^2\, |\boldsymbol{\omega}_i|^2\, \Delta t^4 \left(28r^2 - 20\Delta t\, |\boldsymbol{v}_i|\, r + 5\Delta t^2\, |\boldsymbol{v}_i|^2\right)\left(2r - \Delta t\, |\boldsymbol{v}_i|\right)^2}{128m\, r^2}\,. \tag{40}$$

The second term becomes zero when $\boldsymbol{\omega}_i = 0$ and (14) is recovered for the truncation error. Whether the addition of this second term increases or decreases the error depends solely on the sign of $\left(28r^2 - 20\Delta t\, |\boldsymbol{v}_i|\, r + 5\Delta t^2\, |\boldsymbol{v}_i|^2\right)$: a quadratic equation in terms of r (or $\Delta t\, |\boldsymbol{v}_i|$) with complex roots. The interparticle overlap is restricted to small values to remain physically reasonable [36], particularly in a single time-step. Hence, $|\boldsymbol{U}_n| = \Delta t\, |\boldsymbol{v}_i| \ll r$ so the second term in (40) is invariably positive. Thus, the use of frictional particles and the development of shear forces increases the truncation error in the energy balance for a linear contact model.

The foregoing analysis assumes that the friction limit has not been reached. If this is not the case, (38) must be included in the energy balance. The shear force is rescaled immediately after the forces are updated in the velocity-Verlet integration scheme (27), i.e., before the velocities are updated at the end of the time-step (28, 29). The shear force before rescaling is unchanged from (32); this is

Copyright © 0000 John Wiley & Sons, Ltd.

DOI: 10.1002/nme

relabelled $\boldsymbol{f}^s_{\alpha,\text{old}}$ to avoid confusion. Hence,

$$\boldsymbol{f}^s_{\alpha,t+\Delta t} = \mu\, \boldsymbol{f}^n_{\alpha,t+\Delta t} \tag{41}$$

$$\boldsymbol{f}^s_{\alpha,\text{old}} = -k_s\, \boldsymbol{U}_s = -k_s\, \boldsymbol{\omega}_i\, \Delta t \left(\frac{\boldsymbol{x}_{\beta,t+\Delta t} - \boldsymbol{x}_{\alpha,t+\Delta t}}{2} \right) . \tag{32}$$

$\overline{\boldsymbol{f}^s_{t+\Delta t}}$ is given by the average of the shear forces at the beginning and end of the time-step:

$$\overline{\boldsymbol{f}^s_{t+\Delta t}} = \frac{\boldsymbol{f}^s_{\alpha,t} + \boldsymbol{f}^s_{\alpha,t+\Delta t}}{2} = \frac{\boldsymbol{f}^s_{\alpha,t+\Delta t}}{2} . \tag{42}$$

For a linear contact model, $\boldsymbol{U}^s_s$ is easily found as the difference between unscaled and rescaled shear forces divided by contact shear stiffness. Therefore,

$$\boldsymbol{U}^s_s = \frac{\boldsymbol{f}^s_{\alpha,t+\Delta t} - \boldsymbol{f}^s_{\alpha,\text{old}}}{k_s} \tag{43}$$

$$E^F_{t+\Delta t} = \left| \overline{\boldsymbol{f}^s_{t+\Delta t}}\, \boldsymbol{U}^s_s \right| = \left| \frac{\boldsymbol{f}^s_{\alpha,t+\Delta t} \left(\boldsymbol{f}^s_{\alpha,t+\Delta t} - \boldsymbol{f}^s_{\alpha,\text{old}} \right)}{2k_s} \right| . \tag{44}$$

The analysis proceeds as before to obtain the analytical expression for ϵ:

$$\epsilon = \frac{k_n^2\, |\boldsymbol{v}_i|^2\, \Delta t^4}{4m} + \frac{\mu^2\, k_n^2\, |\boldsymbol{v}_i|^2\, \Delta t^4}{32m\, r^2} \left(28r^2 - 20\Delta t\, |\boldsymbol{v}_i|\, r + 5\Delta t^2\, |\boldsymbol{v}_i|^2 \right) . \tag{45}$$

Only the first term, i.e., (14), remains when $\mu \to 0$. Interestingly, $|\boldsymbol{\omega}_i|$ does not appear in (45). It is unclear by inspecting (40) and (45) whether reaching the Coulomb friction limit increases or decreases ϵ. Defining the ratio of these errors, (45)/(40), as ϵ_r, Figure 5 plots $|\epsilon_r|$ against μ using the following parameters: $\rho = 2650\,\text{kg}\,\text{m}^{-3}$, $r = 3.97 \times 10^{-4}$ m, $k_n = k_s = 1\,\text{MN}\,\text{m}^{-1}$, $|\boldsymbol{v}_i| = 1\,\text{m}\,\text{s}^{-1}$, $|\boldsymbol{\omega}_i| = 1\,\text{s}^{-1}$ and $\Delta t = 1 \times 10^{-8}$ s. $|\epsilon_r|$ increases monotonically as μ is increased. As $\mu \to 0$, $|\epsilon_r| \to 1$ as expected.

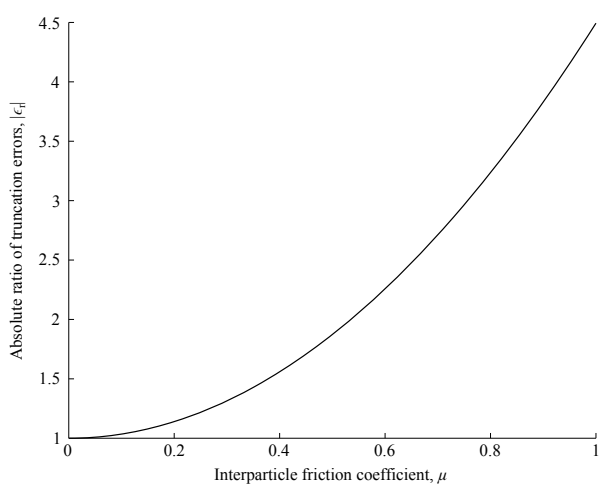

Figure 5. The variation of the absolute ratio of the truncation errors with the interparticle friction coefficient, μ, in one time-step when the Coulomb friction limit is reached (45) and is not reached (40).

Copyright © 0000 John Wiley & Sons, Ltd.

DOI: 10.1002/nme

2.5. *Considering shear forces between frictional particles: Hertzian contact model*

The equivalent analysis for a Hertzian contact model is very similar. (33–36) remain valid and the required velocity-Verlet equations are (24–29). For a Hertzian contact model, $\boldsymbol{f}^{n}_{\alpha,t+\Delta t}$ and $E^{NS}_{t+\Delta t}$ are given by (17) and (18), respectively. The moment terms at time $t+\Delta t$ are both equal to (30), as for the linear contact model. The major difference compared to the linear case is that the contact shear stiffness is a function of interparticle overlap (noting that tangent and secant stiffnesses are equivalent for one time-step). This requires the shear force and the shear component of strain energy to be calculated differently:

$$\boldsymbol{f}^{s}_{\alpha,t+\Delta t} = -\boldsymbol{f}^{s}_{\beta,t+\Delta t} = -H_s\,\boldsymbol{U}_s\sqrt{|\boldsymbol{U}_n|} \tag{46}$$

$$E^{SS}_{t+\Delta t} = \frac{1}{2}\,|\boldsymbol{U}_s\,\boldsymbol{f}^{s}_{\alpha,t+\Delta t}|\,. \tag{47}$$

H_s, like H_n (19), is a function of the particle radii, G and ν:

$$H_s = \frac{4\,G}{2-\nu}\sqrt{\frac{r_\alpha\,r_\beta}{r_\alpha+r_\beta}} = \frac{4\,G}{2-\nu}\sqrt{\frac{r}{2}} \quad \text{if } r_\alpha = r_\beta = r\,.$$

(47) can also be used for the linear analysis instead of (37) but is slightly less convenient in practice. Assuming no energy is dissipated by friction,

$$\epsilon = \frac{H_n^2\,|\boldsymbol{v}_i|^3\,\Delta t^5}{4m} - \frac{1}{10}\,H_n\,(\Delta t\,|\boldsymbol{v}_i|)^{\frac{5}{2}} + \frac{H_s^2\,|\boldsymbol{v}_i|\,|\boldsymbol{\omega}_i|^2\,\Delta t^5\left(28r^2 - 20\Delta t\,|\boldsymbol{v}_i|\,r + 5\Delta t^2\,|\boldsymbol{v}_i|^2\right)(2r-\Delta t\,|\boldsymbol{v}_i|)^2}{128m\,r^2}\,. \tag{48}$$

The final term of (48) becomes zero when $\boldsymbol{\omega}_i = 0$ and (22) is recovered. This final term is very similar to that for a linear contact model (40). Using a similar argument, it again follows that the truncation error in the energy balance is increased by the development of shear forces.

3. TOTAL ERROR ACCRUED IN A SIMULATION

In Section 2, expressions were developed for the truncation error at one contact during one loading time-step. Taking the simple base case as an example, the temptation exists to estimate the total truncation error for a simulation by multiplying (14) by both the number of interparticle contacts and the number of time-steps. This would provide an unreasonably large upper-bound on total truncation error as most of the error accrued during loading cancels out when unloading occurs.

Consider the unloading analogue of the base case shown in Figure 6. The initial configuration is the same as the base case at time $t+\Delta t$, except the signs of the velocity terms are reversed because

Copyright © 0000 John Wiley & Sons, Ltd.

DOI: 10.1002/nme

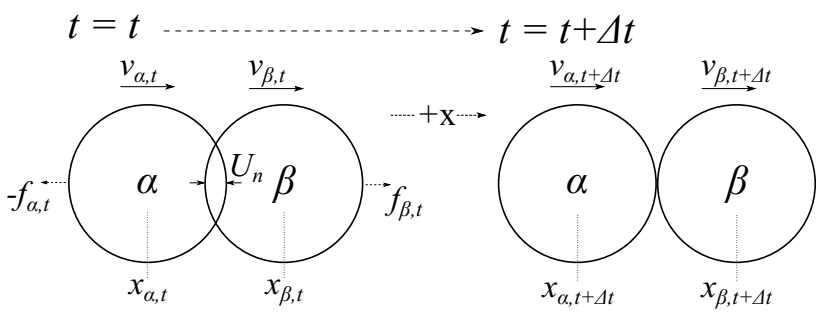

Figure 6. Analogue of the two-particle base case for unloading.

the particles are separating:

$$\begin{aligned}
\boldsymbol{f}^n_{\alpha,t} &= -\boldsymbol{f}^n_{\beta,t} = -k_n\,\Delta t\,\boldsymbol{v}_i \\
\boldsymbol{v}_{\alpha,t} &= -\boldsymbol{v}_i\left(1-\frac{k_n\,\Delta t^2}{2m}\right) \\
\boldsymbol{v}_{\beta,t} &= -\frac{\boldsymbol{v}_i\,k_n\,\Delta t^2}{2m}\ .
\end{aligned}$$

Applying the basic velocity-Verlet equations:

$$\begin{aligned}
\boldsymbol{v}_{\alpha,t+\frac{\Delta t}{2}} &= \boldsymbol{v}_{\alpha,t+\Delta t} = -\boldsymbol{v}_i \\
\boldsymbol{v}_{\beta,t+\frac{\Delta t}{2}} &= \boldsymbol{v}_{\beta,t+\Delta t} = 0 \\
\boldsymbol{x}_{\alpha,t+\Delta t} &= \boldsymbol{x}_{\alpha,t} - \Delta t\,\boldsymbol{v}_i \\
\boldsymbol{x}_{\beta,t+\Delta t} &= \boldsymbol{x}_{\beta,t}\ .
\end{aligned}$$

The particles are again in touching contact at time $t+\Delta t$. The energy balance is

$$E^K_{\alpha,t} + E^K_{\beta,t} + E^{NS}_t = E^K_{\alpha,t+\Delta t} - \epsilon\ .$$

By comparing with (5–9), the truncation error is the reverse of (14), i.e.,

$$\epsilon = -\frac{k_n^2\,|\boldsymbol{v}_i|^2\,\Delta t^4}{4m} \tag{49}$$

This result implies that the truncation error terms will simply cancel out in a load–unload cycle. Unfortunately, a perfect cancellation of positive and negative error terms does not occur in practice for several reasons. Most DEM simulations do not involve perfectly symmetrical load reversals. The truncation errors are path-dependent and the loading and unloading phases will generally contain different numbers of time-steps. In some simulations, there may be a loading phase without a corresponding unloading phase (e.g., simulating the triaxial shearing of a granular soil). A good illustration of the non-cancellation of the truncation errors is gained by considering what happens in a two-particle system with a fixed overlap in which one of the particles has an angular velocity $\boldsymbol{\omega}_i$ and there is no mechanism for energy dissipation. As one particle slows, the other increases in angular velocity. The angular velocities of both particles oscillate out of phase between $\pm\boldsymbol{\omega}_i$ but

Copyright © 0000 John Wiley & Sons, Ltd.

DOI: 10.1002/nme

the accumulated error continually increases in magnitude. This makes it difficult to determine a reasonable upper bound for the accrued truncation error.

4. COMPLICATIONS OF THE BASIC DEM

The simplest two-particle cases were considered in Section 2. In a real granular system, particles have multiple simultaneous contacts and features such as damping or interparticle bonding are often included in the model. In this Section, these three complications of the base case are considered.

4.1. Consideration of multiple contacts

Consider those seven highly-idealised configurations of particles shown in Figure 7. Particle β is stationary at time t while each of the multiple α particles is initially in touching contact with β and has a speed $|\boldsymbol{v}_i|$. Hence, all contact forces are identical in magnitude although different net forces act on the particles. Using the same approach based on energy balances as before, the truncation errors for these seven cases are given in Table I. Both linear and Hertzian contact models were used in the analysis of case *b*.

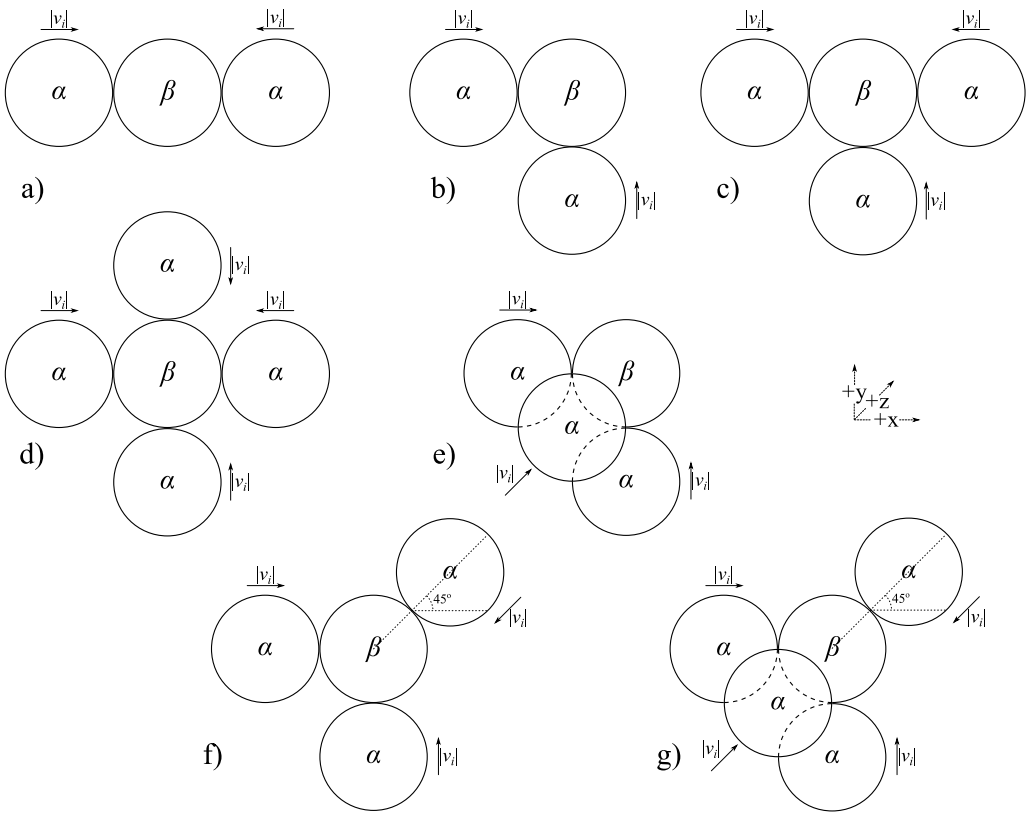

Figure 7. The seven cases considered for multiple simultaneous contacts with particle β shown at time t.

The truncation errors in Table I depend on the net forces acting on the contacting particles; firstly, the net forces are resolved so that they are aligned with the branch vector and then the differences between these resolved forces are summed for all contacts. The resulting summed force

Copyright © 0000 John Wiley & Sons, Ltd.

DOI: 10.1002/nme

Table I. Truncation errors calculated for the seven cases shown in Figure 7 where N_c is the number of contacts. The final column contains a comparison with the two-particle base cases given by (14) and (22).

Case	N_c	Truncation error, ϵ	Comparison with base case
a	2	$\dfrac{k_n^2 \, \lvert \boldsymbol{v}_i \rvert^2 \, \Delta t^4}{4m}$	$1 \times$ (14)
b (linear)	2	$\dfrac{k_n^2 \, \lvert \boldsymbol{v}_i \rvert^2 \, \Delta t^4}{2m}$	$2 \times$ (14)
b (Hertz)	2	$\dfrac{H_n^2 \, \lvert \boldsymbol{v}_i \rvert^3 \, \Delta t^5}{2m} - \dfrac{1}{5} \, H_n \left(\Delta t \, \lvert \boldsymbol{v}_i \rvert \right)^{\frac{5}{2}}$	$2 \times$ (22)
c	3	$\dfrac{k_n^2 \, \lvert \boldsymbol{v}_i \rvert^2 \, \Delta t^4}{2m}$	$2 \times$ (14)
d	4	$\dfrac{k_n^2 \, \lvert \boldsymbol{v}_i \rvert^2 \, \Delta t^4}{2m}$	$2 \times$ (14)
e	3	$\dfrac{3 \, k_n^2 \, \lvert \boldsymbol{v}_i \rvert^2 \, \Delta t^4}{4m}$	$3 \times$ (14)
f	3	$\dfrac{\left(3 - \sqrt{2}\right) k_n^2 \, \lvert \boldsymbol{v}_i \rvert^2 \, \Delta t^4}{4m}$	$\left(3 - \sqrt{2}\right) \times$ (14)
g	4	$\dfrac{\left(4 - \sqrt{2}\right) k_n^2 \, \lvert \boldsymbol{v}_i \rvert^2 \, \Delta t^4}{4m}$	$\left(4 - \sqrt{2}\right) \times$ (14)

is proportional to ϵ. This is illustrated in Figure 8 for three cases: *a*, *b* and *f*. For clarity, let $|\boldsymbol{f}|$ represent the magnitude of the contact force. For case *a*, the net force acting on both α particles has a magnitude $|\boldsymbol{f}|$ while there is no net force on β. The summed difference in net force magnitudes is $2|\boldsymbol{f}|$: the same as for the two-particle base case. Hence, the truncation error is also the same as for the base case. For case *b*, there are force differences of $2|\boldsymbol{f}|$ in both the x- and y-directions: a total of $4|\boldsymbol{f}|$, and so ϵ is twice the value for the base case. Case *f* requires forces to be resolved along the branch vectors joining the particle centroids as shown in Figure 8. Once the net forces have been resolved, the differences at the three contacts are $2|\boldsymbol{f}| - \frac{|\boldsymbol{f}|}{\sqrt{2}}$ (at two contacts) and $2|\boldsymbol{f}| - \sqrt{2}|\boldsymbol{f}|$. The sum is $6|\boldsymbol{f}| - 2\sqrt{2}|\boldsymbol{f}|$, which is a multiple of $\left(3 - \sqrt{2}\right)$ of the base case value of $2|\boldsymbol{f}|$. ϵ for case *f* is the same multiple of (14).

Adding non-collinear contacts to particle β increases the total truncation error in the energy balance. The relationship is clearly dependent on the specific configuration of the contacts: doubling the number of contacts, N_c, does not necessarily double ϵ. Because 3D simulations have larger coordination numbers than the equivalent 2D simulations, the accumulated truncation error is expected to be larger. However, Table I implies that the average truncation error per contact may be similar in 2D and in 3D.

4.2. Damping

Two forms of damping are considered in this paper: local and viscous damping. Both are widely used and are options in DEM codes such as PFC2D/3D [27, 28]. Although both add additional damping forces to the system, there are two main differences between these forms of damping:

1. Local damping acts on a particle; viscous damping acts at a contact.

Copyright © 0000 John Wiley & Sons, Ltd.

DOI: 10.1002/nme

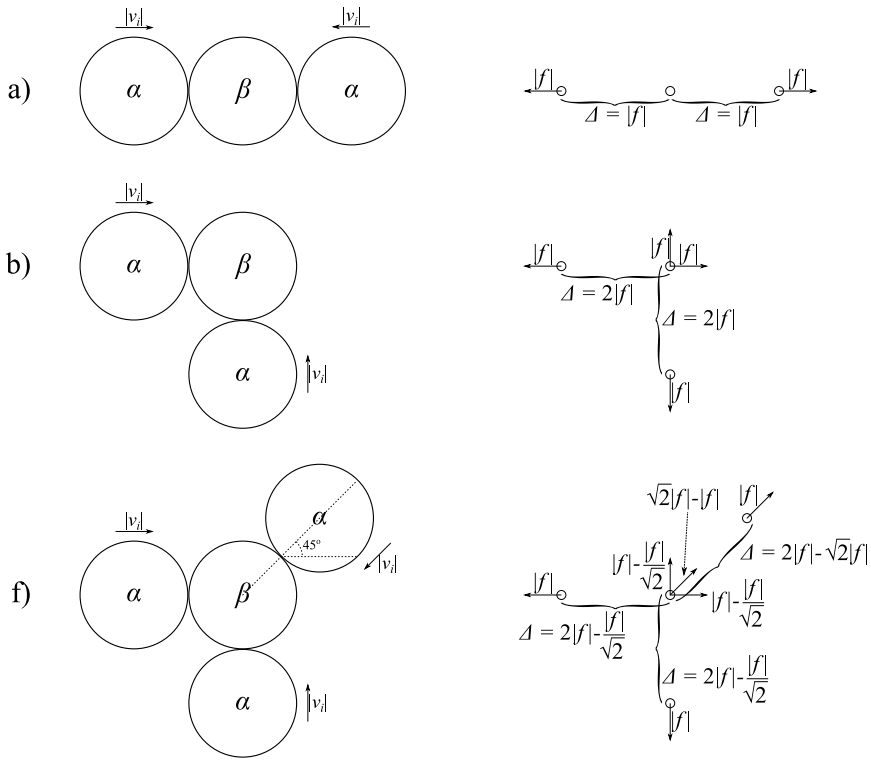

Figure 8. Magnitudes of the net forces acting on particles α and β for three of the cases shown in Figure 7: cases *a*, *b* and *f*.

2. The local damping force is proportional to the unbalanced force (i.e., the particle acceleration force) on a particle [36]; the viscous damping force is proportional to the relative velocity at a contact.

4.2.1. Local damping The only active force in the base case is the normal contact force between particles α and β: $\boldsymbol{f}^n_{\alpha,t+\Delta t} = -\boldsymbol{f}^n_{\beta,t+\Delta t} = -k_n\,\Delta t\,\boldsymbol{v}_i$. Since local damping acts at the particle scale, it affects neither these contact forces nor the strain energy. However, the net forces acting on particles α and β become [28]

$$\boldsymbol{f}_{\alpha,t+\Delta t} = \boldsymbol{f}^n_{\alpha,t+\Delta t} - \gamma_l \left|\boldsymbol{f}^n_{\alpha,t+\Delta t}\right| \operatorname{sgn} \boldsymbol{v}_{\alpha,t+\frac{\Delta t}{2}} = \boldsymbol{f}^n_{\alpha,t+\Delta t}\,(1+\gamma_l)$$
$$\boldsymbol{f}_{\beta,t+\Delta t} = \boldsymbol{f}^n_{\beta,t+\Delta t} - \gamma_l \left|\boldsymbol{f}^n_{\beta,t+\Delta t}\right| \operatorname{sgn} \boldsymbol{v}_{\beta,t+\frac{\Delta t}{2}} = \boldsymbol{f}^n_{\beta,t+\Delta t}\,.$$

γ_l is a dimensionless local damping coefficient. Since the contact force and velocity are opposed for α, the inclusion of local damping increases the magnitude of $\boldsymbol{f}_{\alpha,t+\Delta t}$. Local damping is also applicable to rotational degrees of freedom in cases where these are non-zero. The energy balance is the same as (5) with the addition of one extra term, $E^D_{t+\Delta t}$: the energy dissipated by damping.

$$E^K_{\alpha,t} = E^K_{\alpha,t+\Delta t} + E^K_{\beta,t+\Delta t} + E^{NS}_{t+\Delta t} + E^D_{t+\Delta t} - \epsilon \tag{50}$$

$E^D_{t+\Delta t}$ is calculated for each particle as the magnitude of damping force multiplied by the increment of displacement. Since $(\boldsymbol{x}_{\beta,t+\Delta t} - \boldsymbol{x}_{\beta,t})$ and the contribution of damping to $\boldsymbol{f}_{\beta,t+\Delta t}$ are both zero,

Copyright © 0000 John Wiley & Sons, Ltd.

DOI: 10.1002/nme

particle β does not contribute to (51).

$$E^D_{t+\Delta t} = \gamma_l \left|\boldsymbol{f}^n_{\alpha,t+\Delta t}\right| \Delta t \left|\boldsymbol{v}_{\alpha,t+\frac{\Delta t}{2}}\right| = \gamma_l \, k_n \, \Delta t^2 \left|\boldsymbol{v}_i\right|^2 \tag{51}$$

The truncation error when local damping is active is

$$\epsilon = \frac{k_n^2 \left|\boldsymbol{v}_i\right|^2 \Delta t^4}{4m} + \frac{\gamma_l \, k_n \left|\boldsymbol{v}_i\right|^2 \Delta t^2}{8m} \left(4m + k_n \, \Delta t^2 \left(\gamma_l + 2\right)\right) \ . \tag{52}$$

Since $\gamma_l \geq 0$, the inclusion of local damping increases the truncation error in the energy balance.

4.2.2. Viscous damping The viscous damping term is a multiplier of relative velocity which opposes motion [28]. Viscous damping acts at a contact and therefore affects the contact forces and strain energy:

$$\begin{aligned}
\boldsymbol{f}^n_{\alpha,t+\Delta t} &= -k_n \, \Delta t \, \boldsymbol{v}_i - \gamma_v \left(\boldsymbol{v}_{\alpha,t+\frac{\Delta t}{2}} - \boldsymbol{v}_{\beta,t+\frac{\Delta t}{2}}\right) = -\boldsymbol{v}_i \left(\gamma_v + k_n \, \Delta t\right) \\
\boldsymbol{f}^n_{\beta,t+\Delta t} &= k_n \, \Delta t \, \boldsymbol{v}_i - \gamma_v \left(\boldsymbol{v}_{\beta,t+\frac{\Delta t}{2}} - \boldsymbol{v}_{\alpha,t+\frac{\Delta t}{2}}\right) = -\boldsymbol{f}^n_{\alpha,t+\Delta t} \ .
\end{aligned}$$

γ_v is a viscous damping coefficient which has SI units of kg s^{-1}. (50) is also applicable for viscous damping for which $E^D_{t+\Delta t}$ is substituted by

$$E^D_{t+\Delta t} = \gamma_v \left|\boldsymbol{v}_i\right| \Delta t \left|\boldsymbol{v}_{\alpha,t+\frac{\Delta t}{2}}\right| = \gamma_v \left|\boldsymbol{v}_i\right|^2 \Delta t \ .$$

The truncation error when viscous damping is active is

$$\epsilon = \frac{k_n^2 \left|\boldsymbol{v}_i\right|^2 \Delta t^4}{4m} + \frac{\gamma_v \left|\boldsymbol{v}_i\right|^2}{4m \, k_n} \left(2\gamma_v \, m + k_n \, \Delta t \left(6m + 2k_n \, \Delta t^2 + \gamma_v \, \Delta t\right)\right) \ . \tag{53}$$

As in (52), the second term of (53) is positive so the inclusion of viscous damping increases ϵ.

4.3. Interparticle bonding

The fundamental particles in DEM are sometimes bonded together, e.g., to simulate crushable agglomerates [37–39]. The two most common types of interparticle bond are contact bonds and parallel bonds [28, 36].

4.3.1. Contact bond Contact bonds are the simpler of these two types. They consist of two orthogonal springs at a contact in the normal and tangential directions [28]. Contact bonds are capable of transmitting only forces, not moments. Only the normal component is active in the base case. This component of the contact bond can be envisioned as a linear contact spring which is active only in tension (i.e., when the particles are not in contact: $\boldsymbol{U}_n < 0$). The force imposed on the particles therefore becomes

$$\boldsymbol{f}^n_{\alpha,t+\Delta t} = -\boldsymbol{f}^n_{\beta,t+\Delta t} = -k_n \, \boldsymbol{U}_n \quad \forall \, \boldsymbol{U}_n \ .$$

Copyright © 0000 John Wiley & Sons, Ltd.

DOI: 10.1002/nme

It is usual for the normal contact spring (active in compression) and the normal contact bond (active in tension) to have the same stiffness. The contact bond has a finite strength: when the magnitude of $\boldsymbol{f}^n_{\alpha,t+\Delta t}$ exceeds a limiting value in tension, the bond breaks and $\boldsymbol{f}^n_{\alpha,t+\Delta t}$ is instantaneously reduced to 0.

Consider the modification of the base case shown in Figure 9. The particle velocities at time t are reversed compared to the base case (i.e., $\boldsymbol{v}_{\alpha,t} = -\boldsymbol{v}_i$; $\boldsymbol{v}_{\beta,t} = 0$) so that a separation of the particles occurs during the time-step $t \to t + \Delta t$. The energy balance is identical to (10) where the strain energy now applies to the contact bond rather than the normal contact spring. If it is assumed that the strength of the contact bond has not been reached at time $t + \Delta t$, (14) is obtained for ϵ. The truncation error is the same in tension prior to bond failure as in compression. Once bond failure occurs, the strain energy can be tracked as bond failure energy.

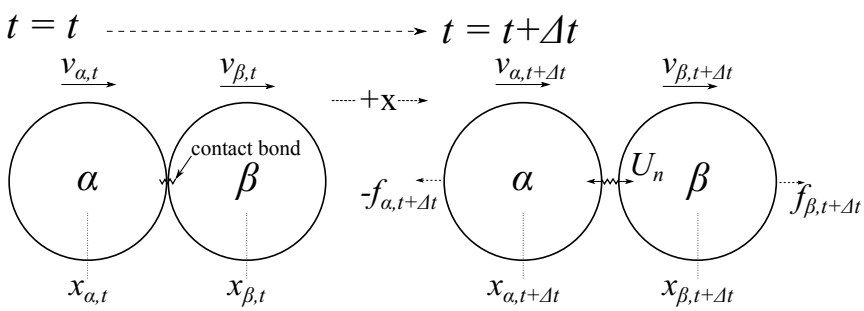

Figure 9. Modification of the two-particle base case shown in Figure 1 to give a separation of the particles by time $t + \Delta t$.

4.3.2. Parallel bond Parallel bonds bonds transmit both forces and moments [28, 36]. They are so-called because they act in parallel with the contact model. Parallel bonds can be envisioned as a thick elastic spring connected rigidly to both particles so that rotating or twisting one of the particles relative to the other generates a torque. Parallel bonds are characterised by five parameters: a bond radius, r_b; a normal and shear strength; a normal stiffness, k_{bn} and a shear stiffness, k_{bs}. The stiffnesses have dimensions of [stress]/[displacement] rather than the more common [force]/[displacement] [40].

Consider again the case shown in Figure 4 in which particle α has an initial angular velocity, $\boldsymbol{\omega}_i$. Add a parallel bond at this contact and assume that neither the normal strength nor the shear strength are reached during the time-step $t \to t + \Delta t$. The forces acting on α and β at time $t + \Delta t$ differ from those in Section 2.4, noting that $\boldsymbol{f}_{\alpha,t} = \boldsymbol{f}_{\beta,t} = 0$:

$$\boldsymbol{f}_{\alpha,t+\Delta t} = -\boldsymbol{f}_{\beta,t+\Delta t} = \boldsymbol{f}_{\alpha,t} + \boldsymbol{f}^n_{\alpha,t+\Delta t} + \boldsymbol{f}^s_{\alpha,t+\Delta t} + \boldsymbol{f}^{bn}_{\alpha,t+\Delta t} + \boldsymbol{f}^{bs}_{\alpha,t+\Delta t} \, .$$

$\boldsymbol{f}^{bn}_{\alpha,t+\Delta t}$ and $\boldsymbol{f}^{bs}_{\alpha,t+\Delta t}$ are the contributions of the parallel bond to the net force on α in the normal and orthogonal directions to the branch vector. Since this is a two-dimensional problem, these forces are calculated using a simplification of the general three-dimensional equations [27, 36]:

$$\boldsymbol{f}^{bn}_{\alpha,t+\Delta t} = -\boldsymbol{f}^{bn}_{\beta,t+\Delta t} = -k_{bn}\, \pi\, r_b^2\, \boldsymbol{U}_n$$
$$\boldsymbol{f}^{bs}_{\alpha,t+\Delta t} = \boldsymbol{f}^{bs}_{\beta,t+\Delta t} = k_{bs}\, \pi\, r_b^2\, \boldsymbol{U}_s \, .$$

Copyright © 0000 John Wiley & Sons, Ltd.

DOI: 10.1002/nme

The moment terms must also be modified from (30, 31):

$$\boldsymbol{M}_{\alpha,t+\Delta t} = \boldsymbol{f}^s_{\alpha,t+\Delta t}\left(\frac{\boldsymbol{x}_{\beta,t+\Delta t} - \boldsymbol{x}_{\alpha,t+\Delta t}}{2}\right) - \boldsymbol{M}^b_{\beta,t+\Delta t}$$
$$\boldsymbol{M}_{\beta,t+\Delta t} = \boldsymbol{f}^s_{\alpha,t+\Delta t}\left(\frac{\boldsymbol{x}_{\beta,t+\Delta t} - \boldsymbol{x}_{\alpha,t+\Delta t}}{2}\right) + \boldsymbol{M}^b_{\beta,t+\Delta t}$$

where the contribution of the parallel bond to moment is

$$\boldsymbol{M}^b_{\beta,t+\Delta t} = \frac{\pi}{4}\, k_{bn}\, r_b^4\, \Delta t\, \boldsymbol{\omega}_i\ .$$

The energy balance when a parallel bond is included, assuming that frictional sliding does not occur, is

$$E^K_{\alpha,t} = E^K_{\alpha,t+\Delta t} + E^K_{\beta,t+\Delta t} + E^{NS}_{t+\Delta t} + E^{SS}_{t+\Delta t} + E^B_{t+\Delta t} - \epsilon \tag{54}$$

where $E^{NS}_{t+\Delta t}$ and $E^{SS}_{t+\Delta t}$ are calculated using (9) and (37), as in Section 2.4 and $E^B_{t+\Delta t}$ is the strain energy stored in the parallel bond. This is calculated as (55) for this two-dimensional case [27]:

$$E^B_{t+\Delta t} = \frac{1}{2}\left(\frac{\left|\boldsymbol{f}^{bn}_{\alpha,t+\Delta t}\right|^2}{\pi\, r_b^2\, k_{bn}} + \frac{\left|\boldsymbol{f}^{bs}_{\alpha,t+\Delta t}\right|^2}{\pi\, r_b^2\, k_{bs}} + 4\,\frac{\left|\boldsymbol{M}^b_{\alpha,t+\Delta t}\right|^2}{\pi\, r_b^4\, k_{bn}}\right)\ . \tag{55}$$

Solving (54) for ϵ gives the following cumbersome solution:

$$\begin{aligned}\epsilon = \frac{k_n^2\,|\boldsymbol{v}_i|^2\,\Delta t^4}{4m} + \frac{k_s^2\,|\boldsymbol{\omega}_i|^2\,\Delta t^4\left(28r^2 - 20\Delta t\,|\boldsymbol{v}_i|\,r + 5\Delta t^2\,|\boldsymbol{v}_i|^2\right)\left(2r - \Delta t\,|\boldsymbol{v}_i|\right)^2}{128m\,r^2} + \frac{\pi\,\Delta t^2\,r_b^2}{128m\,r^2}\Big(\\ k_{bs}\,\Delta t^2\,|\boldsymbol{\omega}_i|^2\left(\pi\,k_{bs}\,r_b^2 - 2k_s\right)\left(5|\boldsymbol{v}_i|^4\,\Delta t^4 - 40|\boldsymbol{v}_i|^3\,\Delta t^3\,r + 128|\boldsymbol{v}_i|^2\,\Delta t^2\,r^2 - 192|\boldsymbol{v}_i|\,\Delta t\,r^3 + 112r^4\right)\\ + 32|\boldsymbol{v}_i|^2\,\Delta t^2\,r^2\left(|\boldsymbol{\omega}_i|^2\,k_{bs}\,m + \pi\,r_b^2\,k_{bn}^2 + 2k_n\,k_{bn}\right)\\ + 5\pi\,|\boldsymbol{\omega}_i|^2\,\Delta t^2\,k_{bn}^2\,r_b^6 + 128m\,r^3\,|\boldsymbol{\omega}_i|^2\,k_{bs}(r - \Delta t|\boldsymbol{v}_i|)\Big)\ .\end{aligned} \tag{56}$$

The first two terms in this expression are identical to (40) showing that this is recovered if the bond radius, r_b, is set to zero.

5. EFFECTS OF TIME-STEP AND DENSITY SCALING ON TRUNCATION ERROR

Consider the dependence of truncation error, ϵ, on the simulation time-step, Δt. Table II summarises this for the four main two-particle cases in Section 2. The last three entries in Table II have equations for ϵ that contain several different relationships with Δt, e.g., (21) for the Hertzian contact model without shear forces contains two terms: one proportional to $\Delta t^{\frac{5}{2}}$ and the other proportional to Δt^5. Table II shows both the lowest- and highest-order dependencies.

ϵ invariably has a superlinear relationship with Δt. Therefore, it follows that reducing the simulation time-step will reduce the truncation error substantially. Consider as an example the case of the linear contact model without shear force for which $\epsilon \propto \Delta t^4$. Suppose the time-step is halved from Δt_s (15) to $\frac{1}{2}\Delta t_s$. The number of time-steps needed to simulate any given time period is doubled, but the truncation error per time-step is reduced by a factor of 16. If it is assumed that the

Copyright © 0000 John Wiley & Sons, Ltd.

DOI: 10.1002/nme

Table II. Summary of the dependence of the truncation errors on time-step for the four main two-particle cases identified in Section 2: linear and Hertzian contact models, with and without shear force.

Contact model	Shear force?	Equation	Dependence on Δt
Linear	No	(14)	$\epsilon \propto \Delta t^4$
Linear	Yes	(40)	$\epsilon \propto \Delta t^4$ — $\epsilon \propto \Delta t^8$
Hertz	No	(21)	$\epsilon \propto \Delta t^{\frac{5}{2}}$ — $\epsilon \propto \Delta t^5$
Hertz	Yes	(48)	$\epsilon \propto \Delta t^{\frac{5}{2}}$ — $\epsilon \propto \Delta t^9$

Table III. Dependence of ϵ on ρ for the four main two-particle cases identified in Section 2.

Contact model	Shear force?	Equation	Dependence on ρ
Linear	No	(14)	$\epsilon \propto \rho$
Linear	Yes	(40)	$\epsilon \propto \rho$ — $\epsilon \propto \rho^3$
Hertz	No	(21)	$\epsilon \propto \rho^{\frac{5}{4}}$ — $\epsilon \propto \rho^{\frac{3}{2}}$
Hertz	Yes	(48)	$\epsilon \propto \rho^{\frac{5}{4}}$ — $\epsilon \propto \rho^{\frac{7}{2}}$

accrued error is correlated with the sum of the truncation errors for each time-step (notwithstanding the discussion in Section 3), halving the time-step will reduce the accrued error by a factor of 8.

The truncation error is reduced by reducing Δt; however, the opposite happens to the round-off error which scales with the number of computations [11]. This implies that there is an optimal, implementation-specific choice of Δt which minimises the total error. Generally, if it is assumed that the adopted time-step is the largest value which ensures stability and the code implementation is conventional (no unnecessary computations, double rather than single precision, etc.), the round-off error is smaller than the truncation error by orders of magnitude. It is usually beneficial from an accuracy standpoint to reduce the simulation time-step substantially. In practice, it seems that accuracy tends to be a secondary consideration in large-scale DEM simulations as researchers wish to maximise the time-step to enable more ambitious simulations.

Quasi-static DEM simulations without body forces such as gravity sometimes use a technique known as 'density scaling' to increase the simulation time-step [39, 41–43]. The time required to run a simulation can be greatly reduced by increasing the particle density to physically-unrealistic values (i.e., increasing m in (15)). Consider again the four main two-particle cases in Section 2, focusing on the dependence of ϵ on the particle density, ρ, as shown in Table III. In all of these equations, $m \propto \rho$. For a linear contact model, $\Delta t \propto \sqrt{\rho}$ (15) and the same is true for a Hertzian contact model [35, 41].

Take as an example the linear contact model without shear force for which $\epsilon \propto \rho$. Assume that the particle density is increased from ρ to 100ρ. The truncation error per time-step is increased by a factor of 100 whereas the number of time-steps needed to simulate any fixed time period is increased only ten-fold (15). This means that density scaling has an extremely severe effect on absolute truncation error. If the particle densities are scaled up by 12 orders of magnitude [41, 43], the accrued truncation error for this linear case without shear force increases by a factor of 10^6. The effect of density scaling on accuracy is even more punitive in other cases. For a linear contact model with shear force, the best-case scenario is the same as for the case without shear forces. The worst-case scenario, assuming densities are scaled up by 12 orders of magnitude, is an increase in the accrued truncation error by a factor of 10^{30}.

Copyright © 0000 John Wiley & Sons, Ltd.

DOI: 10.1002/nme

Clearly, the absolute error is greatly increased by the adoption of density scaling. However, the effect on the *relative* error is likely to be of greater importance. The kinetic and strain energy terms in the energy balance also have a dependence on ρ, e.g., $E^K_{\alpha,t} \propto \rho$ and $E^{NS}_{\alpha,t} \propto \Delta t^2 \propto \rho$ for a linear system. This means that the truncation error has the same linear dependence on ρ as the other energy terms in (10). Thus the truncation error for a single time-step, relative to the total energy in the system, is unchanged by density scaling when a linear contact model without shear force is chosen. When simulating a fixed time period, increasing ρ reduces the accrued relative truncation error because fewer time-steps need to be simulated. Unfortunately, this is only true for the simplest case (linear contact model, no shear force). For all other cases, density scaling will increase the accrued relative truncation error.

6. VERIFICATION IN A DEM CODE

One convenient way of verifying the applicability of these analytical solutions is by simulation using a well-regarded DEM code. Simulations were run using the PFC2D 4.00 software [30] with the aim of verifying (14), (16), (40) and (45). Each simulation was run for a single time-step and input parameters were varied individually to investigate the effect on the error. These simulations were exact replicas of the idealised cases considered in this paper, e.g., the simulations used to verify (14) used two identical, frictionless spherical particles which were in touching contact before one of the particles was projected towards the other at a speed $|\boldsymbol{v}_i|$. The error was computed in FISH code based on energy balances. For example, ϵ was quantified in the simulations to verify (14) by rearranging (5):

$$\epsilon = E^K_{\alpha,t+\Delta t} + E^K_{\beta,t+\Delta t} + E^{NS}_{t+\Delta t} - E^K_{\alpha,t} \,. \tag{57}$$

PFC2D is capable of calculating certain energy terms including $E^F_{t+\Delta t}$, $E^K_{\alpha,t}$, $E^{NS}_{t+\Delta t}$ and $E^{SS}_{t+\Delta t}$ [27]. Since PFC2D does not compute strain energy for Hertzian contacts, a linear contact model was used for all verification simulations. One small complication is that the kinetic energy terms at time $t + \Delta t$ are not computed in PFC2D; this is because the Verlet-based integration scheme in PFC2D calculates particle velocities only at half-time-step intervals (i.e., $t + \frac{\Delta t}{2}$, $t + \frac{3\Delta t}{2}$, ...). For verification purposes, (28), (29), (35) and (36) were implemented in FISH code to calculate $\boldsymbol{v}_{\alpha/\beta,t+\Delta t}$, $\boldsymbol{\omega}_{\alpha/\beta,t+\Delta t}$, $E^K_{\alpha,t+\Delta t}$ and $E^K_{\beta,t+\Delta t}$, respectively. Finally, the 'PFC ϵ' value was calculated in FISH code, e.g., using (57) to verify (14). These values of simulation error were written to output files in scientific notation and with all available precision to maximise the accuracy of the simulation output. A subset of the 2D simulations were also run in PFC3D 4.00 [44]; the results obtained were identical to those for the 2D simulations. The time-steps used throughout Section 6 are sufficiently small to ensure stability in all cases.

Considering firstly the verification of (14), a standard set of input parameters was defined: k_n = 1 MN m^{-1}, $|\boldsymbol{v}_i|$ = 1 m s^{-1}, r = 3.97 × 10^{-4} m, Δt = 1 × 10^{-8} s and ρ = 2650 kg m^{-3}. The first four of these parameters were separately increased by one order of magnitude (e.g., $|\boldsymbol{v}_i|$ was varied between 1 m s^{-1} and 10 m s^{-1}). Figure 10 compares the analytical truncation error, ϵ, with the error obtained in the PFC2D simulations, and also shows the absolute difference between these on a secondary y-axis. The analytical and simulation errors correspond very closely, with the absolute

Copyright © 0000 John Wiley & Sons, Ltd.

DOI: 10.1002/nme

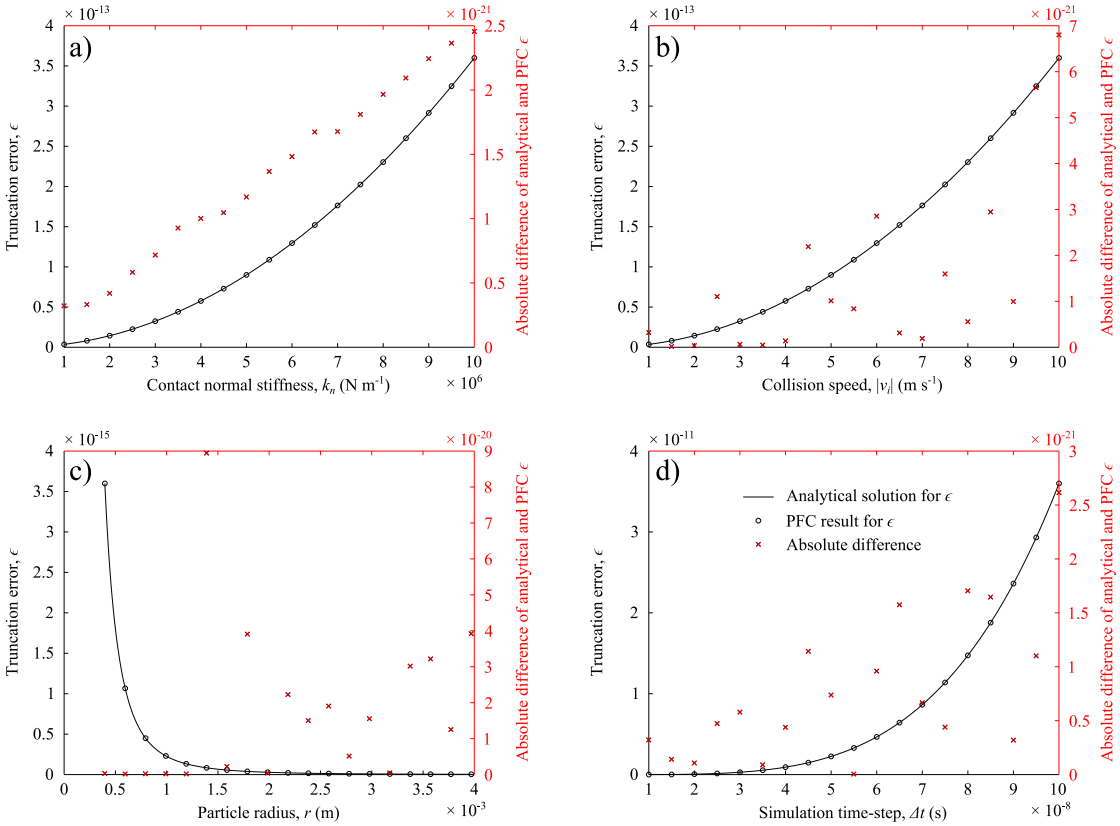

Figure 10. Comparisons of the analytical solution for truncation error, ϵ, given by (14) with the error obtained in PFC2D simulations in which input parameters are varied individually. k_n, $|\boldsymbol{v}_i|$, r and Δt are each varied by one order of magnitude in *a–d*, respectively. The secondary y-axes show the absolute differences between the analytical and simulation errors (in red).

difference between the two being at least five orders of magnitude smaller than ϵ. It is likely that these absolute differences are reasonable upper-bound estimates of the round-off error for these simulations. However, the systematic trends seen in Figure 10a indicate a lack of randomness that one would expect for round-off error. Several of the simulations were run with two different Intel processors (a 2.1 GHz Core i7-4600U and a 2 GHz Atom Z550) and the results obtained were identical.

When validating (16), the main interest was in confirming that the variation of ϵ with R was captured correctly. Figure 11 demonstrates that this is the case for $k_n = 1\,\mathrm{MN\,m^{-1}}$, $|\boldsymbol{v}_i| = 1\,\mathrm{m\,s^{-1}}$, $C = 1.39 \times 10^{-6}\,\mathrm{kg}$ and $\Delta t = 1 \times 10^{-8}\,\mathrm{s}$. The absolute differences are approximately eight orders of magnitude smaller than ϵ. Figure 12 confirms the validity of (40) for the following set of standard input parameters: $k_n = k_s = 1\,\mathrm{MN\,m^{-1}}$, $|\boldsymbol{v}_i| = 1\,\mathrm{m\,s^{-1}}$, $|\boldsymbol{\omega}_i| = 100\,\mathrm{s^{-1}}$, $r = 3.97 \times 10^{-4}\,\mathrm{m}$, $\Delta t = 1 \times 10^{-8}\,\mathrm{s}$ and $\rho = 2650\,\mathrm{kg\,m^{-3}}$. The interparticle friction coefficient for these simulations was set to an arbitrarily large value to ensure that $E^F_{t+\Delta t}$ is zero. In Figure 13, values of μ in the range $0 \leq \mu \leq 1$ were chosen and k_s was increased to $100\,\mathrm{MN\,m^{-1}}$ to ensure that $E^F_{t+\Delta t} > 0$, thus enabling the validation of (45). The absolute differences between the analytical ϵ and PFC2D error values are at least four orders of magnitude smaller than ϵ in all of these analyses.

Copyright © 0000 John Wiley & Sons, Ltd.

DOI: 10.1002/nme

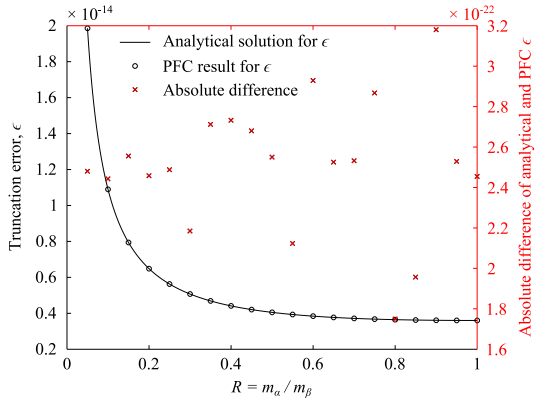

Figure 11. Comparison of the analytical solution for ϵ given by (16) with the error obtained in PFC2D simulations when R is varied and all other input parameters are held constant. Absolute differences are shown in red on a secondary y-axis, as for Figure 10.

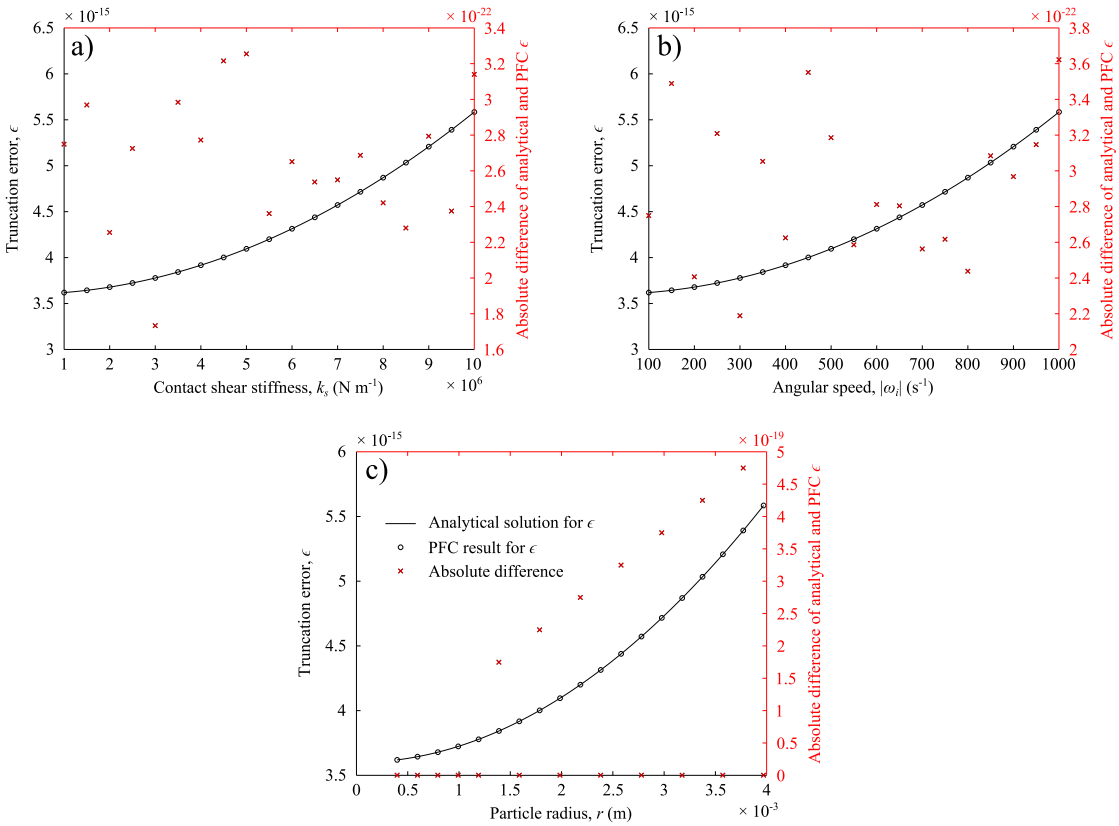

Figure 12. Comparisons of (40) with the error obtained in PFC2D simulations in which k_s, $|\boldsymbol{\omega}_i|$ and r are varied individually. are each varied by one order of magnitude in *a–d*, respectively. Absolute differences are shown in red on the secondary y-axes, as for Figure 10.

7. CONCLUSIONS

In this paper, the truncation error, ϵ, has been quantified for a range of idealised particulate systems by comparing energy balances at the beginning and end of one simulation time-step. Although this analysis explicitly considers only a single time-step, the total accrued truncation error in a simulation

Copyright © 0000 John Wiley & Sons, Ltd.

DOI: 10.1002/nme

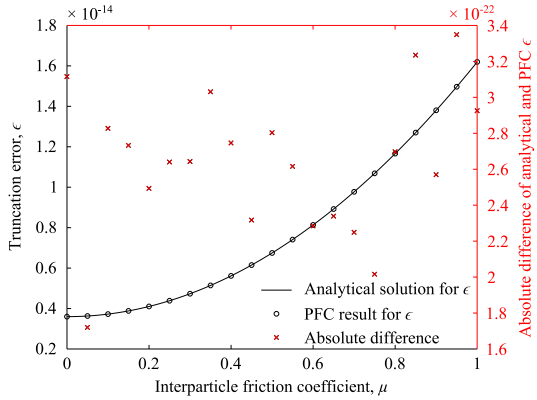

Figure 13. Comparison of (45) with the error obtained in PFC2D simulations when only μ is varied. Absolute differences are shown in red on a secondary y-axis.

necessarily depends on the error in a single step: hence inferences drawn from studies of ϵ are also germane to the accrued error in a simulation containing millions of time-steps. Key expressions obtained for ϵ using this analytical approach were verified by comparison with the commercial DEM software PFC2D. This study focused on the second-order velocity-Verlet integration scheme due to its widespread application in DEM codes.

The truncation error has a superlinear relationship with the simulation time-step, Δt. Reducing Δt substantially reduces ϵ; however, increasing the number of time-steps required in a simulation inevitably increases the round-off error. This implies that there is an optimal, implementation-specific choice of Δt which minimises the total error. By comparing the output of PFC2D simulations with analytical expressions for ϵ, it was confirmed that the round-off error is smaller than the truncation error by orders of magnitude. Therefore, the accuracy of a simulation can generally be improved by choosing a smaller time-step. If the polydispersity of a simulation is increased by including smaller particle sizes, smaller time-steps are necessitated to maintain simulation stability causing ϵ to be reduced.

The adoption of density scaling allows Δt to be increased for a quasi-static simulation with a corresponding reduction of simulation duration. This analysis showed that density scaling massively increases the absolute error. The accrued absolute truncation error increases by a factor of 10^6 when particle densities are increased by a typical scaling factor of 10^{12} for the case of a normal impact of two frictionless particles with a linear contact model. However, the accrued relative truncation error, expressed as a proportion of total energy in the system, may be reduced for the case of a linear contact model without shear force by increasing the particle densities. In addition to particle density and simulation time-step, many other factors influence the truncation error in a simple two-particle system. ϵ scales superlinearly with the collision speed (in a system dominated by collisions) or the strain rate (in a densely-packed system). If the particles are frictional (i.e., $\mu > 0$), ϵ increases with angular speed. The dissipation of energy by friction during a time-step also increases ϵ.

The most common complication of the basic two-particle DEM is the introduction of multiple simultaneous contacts. Increasing the number of non-collinear contacts tends to increase ϵ for a system. This implies that 2D simulations are inherently more accurate than 3D simulations, in the sense of minimising the accrued simulation error, due to the reduced coordination numbers. However, this consideration is usually outweighed by the failure of 2D simulations to capture

Copyright © 0000 John Wiley & Sons, Ltd.

DOI: 10.1002/nme

the real behaviour of a physical, three-dimensional system. Although it depends on the specific configuration of contacts, the average truncation error per contact is similar in 2D and in 3D. Other common complications of the basic DEM include the addition of damping or interparticle bonds. The inclusion of either local or viscous damping increases ϵ while the magnitude of ϵ is the same for a contact bond in tension and for a compressive force caused by interparticle overlap.

REFERENCES

1. Cundall PA, Strack ODL. The distinct element methods as a tool for research in granular media. *Part I, Report to NSF* 1978.
2. Cundall PA, Strack ODL. A discrete numerical model for granular assemblies. *Géotechnique* 1979; **29**:47–65.
3. Di Renzo A, Di Maio FP. Comparison of contact-force models for the simulation of collisions in DEM-based granular flow codes. *Chemical Engineering Science* 2004; **59**:525–541.
4. Thornton C, Cummins SJ, Cleary PW. An investigation of the comparative behaviour of alternative contact force models during inelastic collisions. *Powder Technology* 2013; **233**:30–46.
5. Kuhn MR, Bagi K. Specimen size effect in discrete element simulations of granular assemblies. *Journal of Engineering Mechanics* 2009; **135**:485–492.
6. Plassiard J-P, Belheine N, Donzé F-V. A spherical discrete element model: calibration procedure and incremental response. *Granular Matter* 2009; **11**:293–306.
7. Huang X, Hanley KJ, O'Sullivan C, Kwok FC-Y. Effect of sample size on the response of DEM samples with a realistic grading. *Particuology* 2014; **15**:107–115.
8. Kuo HP, Knight PC, Parker DJ, Tsuji Y, Adams MJ, Seville JPK. The influence of DEM simulation parameters on the particle behaviour in a V-mixer. *Chemical Engineering Science* 2002; **57**:3621–3638.
9. Barreto D, O'Sullivan C. The influence of inter-particle friction and the intermediate stress ratio on soil response under generalised stress conditions. *Granular Matter* 2012; **14**:505–521.
10. Huang X, Hanley KJ, O'Sullivan C, Kwok C-Y. Exploring the influence of interparticle friction on critical state behaviour using DEM. *International Journal for Numerical and Analytical Methods in Geomechanics* 2014; **38**:1276–1297.
11. Press WH, Teukolsky SA, Vetterling WT, Flannery BP. 2007. *Numerical Recipes: The Art of Scientific Computing* (3rd edn). Cambridge University Press.
12. Hoffman JD. 2001. *Numerical Methods for Engineers and Scientists* (2nd edn). CRC Press.
13. Fraige FY, Langston PA. Integration schemes and damping algorithms in distinct element models. *Advanced Powder Technology* 2004; **15**:227–245.
14. Malone KF, Xu BH. Determination of contact parameters for discrete element method simulations of granular systems. *Particuology* 2008; **6**:521–528.
15. Asmar BN, Langston PA, Matchett AJ, Walters JK. Energy monitoring in distinct element models of particle systems. *Advanced Powder Technology* 2003; **14**:43–69.
16. El Shamy U, Denissen C. Microscale characterization of energy dissipation mechanisms in liquefiable granular soils. *Computers and Geotechnics* 2010; **37**:846–857.
17. Burkhart TA, Andrews DM, Dunning CE. Finite element modeling mesh quality, energy balance and validation methods: a review with recommendations associated with the modeling of bone tissue. *Journal of Biomechanics* 2013; **46**:1477–1488.
18. Zhang D, Whiten WJ. An efficient calculation method for particle motion in discrete element simulations. *Powder Technology* 1998; **98**:223–230.
19. Rougier E, Munjiza A, John NWM. Numerical comparison of some explicit time integration schemes used in DEM, FEM/DEM and molecular dynamics. *International Journal for Numerical Methods in Engineering* 2004; **61**:856–879.
20. Kruggel-Emden H, Sturm M, Wirtz S, Scherer V. Selection of an appropriate time integration scheme for the discrete element method (DEM). *Computers and Chemical Engineering* 2008; **32**:2263–2279.
21. Kruggel-Emden H, Stepanek F, Munjiza A. Performance of integration schemes in discrete element simulations of particle systems involving consecutive contacts. *Computers and Chemical Engineering* 2011; **35**:2152–2157.
22. Plimpton S. Fast parallel algorithms for short-range molecular dynamics. *Journal of Computational Physics* 1995; **117**:1–19.

Copyright © 0000 John Wiley & Sons, Ltd.

Prepared using nmeauth.cls
DOI: 10.1002/nme

23. Kloss C, Goniva C, Hager A, Amberger S, Pirker S. Models, algorithms and validation for opensource DEM and CFD-DEM. *Progress in Computational Fluid Dynamics, An International Journal* 2012; **12**:140–152.
24. Šmilauer V, Catalano E, Chareyre B, Dorofeenko S, Duriez J, Gladky A, Kozicki J, Modenese C, Scholtès L, Sibille L, Stránský J, Thoeni K. *Yade Documentation* (1st edn): The Yade Project, 2010. (http://yade-dem.org/doc/).
25. Thornton AR, Weinhart T, Luding S, Bokhove O. Modeling of particle size segregation: Calibration using the discrete particle method. *International Journal of Modern Physics C* 2012; **23**:1240014.
26. Weinhart T, Thornton AR, Luding S, Bokhove O. From discrete particles to continuum fields near a boundary. *Granular Matter* 2012; **14**:289–294.
27. Itasca Consulting Group. 2008. *PFC2D: Particle flow code in two dimensions User's Guide* (4th edn).
28. Itasca Consulting Group. 2008. *PFC3D: Particle flow code in three dimensions User's Guide* (4th edn).
29. Maplesoft. 2013. *Maple v.17.00* (computer software). Waterloo, Ontario, Canada.
30. Itasca Consulting Group. 2008. *PFC2D v.4.00* (computer software). Minneapolis, Minnesota, USA.
31. Belytschko T, Liu WK, Moran B, Elkhodary KI. 2013. *Nonlinear finite elements for continua and structures* (2nd edn). Wiley.
32. Zhang Y, Campbell CS. The interface between fluid-like and solid-like behaviour in two-dimensional granular flows. *Journal of Fluid Mechanics* 1992; **237**:541–568.
33. O'Sullivan C, Bray JD. Selecting a suitable time step for discrete element simulations that use the central difference time integration scheme. *Engineering Computations* 2004; **21**:278–303.
34. Tavarez FA, Plesha ME. Discrete element method for modelling solid and particulate materials. *International Journal for Numerical Methods in Engineering* 2007; **70**:379–404.
35. Li Y, Xu Y, Thornton C. A comparison of discrete element simulations and experiments for 'sandpiles' composed of spherical particles. *Powder Technology* 2005; **160**:219–228.
36. Potyondy DO, Cundall PA. A bonded-particle model for rock. *International Journal of Rock Mechanics and Mining Sciences* 2004; **41**:1329–1364.
37. Thornton C, Ciomocos MT, Adams MJ. Numerical simulations of agglomerate impact breakage. *Powder Technology* 1999; **105**:74–82.
38. Thornton C, Liu L. How do agglomerates break? *Powder Technology* 2004; **143-144**:110–116.
39. Hanley KJ, O'Sullivan C, Byrne EP, Cronin K. Discrete element modelling of the quasi-static uniaxial compression of individual infant formula agglomerates. *Particuology* 2012; **10**:523–531.
40. Cheung LYG. 2008. *Micromechanics of sand production in oil wells* (PhD thesis). Imperial College London.
41. Sheng Y, Lawrence CJ, Briscoe BJ, Thornton C. Numerical studies of uniaxial powder compaction process by 3D DEM. *Engineering Computations* 2004; **21**:304–317.
42. Sykut J, Molenda M, Horabik J. DEM simulation of the packing structure and wall load in a 2-dimensional silo. *Granular Matter* 2008; **10**:273–278.
43. Thornton C. Numerical simulations of deviatoric shear deformation of granular media. *Géotechnique* 2000; **50**:43–53.
44. Itasca Consulting Group. 2008. *PFC3D v.4.00* (computer software). Minneapolis, Minnesota, USA.

Copyright © 0000 John Wiley & Sons, Ltd.

Prepared using nmeauth.cls
DOI: 10.1002/nme